

Initial Trigger Strategy for the P-ONE Detector

by

Santiago Jose Miro Trejo

A thesis submitted in partial fulfillment of the requirements for the degree of

Master of Science

Department of Physics
University of Alberta

© Santiago Jose Miro Trejo, 2024

Abstract

This thesis presents a comprehensive analysis of trigger algorithm efficiency for neutrino event detection in the Pacific Ocean Neutrino Experiment (P-ONE) detector. Investigating muon, electron, and tau neutrinos, the study highlights distinctive interaction characteristics. Beginning with a detailed theoretical background, the research covers the design and components of P-ONE, including the STRAW pathfinder and principles governing muon track and cascade detection. Using a software framework, simulations modeled a muon neutrino flux, monoenergetic muons, and full energy spectra for neutrinos. Trigger algorithm development, reconstructable event selection, and string spacing optimization are discussed. Efficiency analyses, reveal a 70% muon neutrino detection at 10TeV and over 90% efficiency for electron and tau neutrinos at 10TeV. The muon efficiency could also be increased to 85% if a second level trigger algorithm with a factor 50 or more rate reduction can be developed.

Acknowledgements

I would like to express my gratitude to Professor Roger Moore, who supervised and directed this thesis in its entirety. Additionally, I extend my thanks to Professor Carsten Krauss and Professor Juan Pablo Yanez for their co-supervision of this work. I appreciate the valuable assistance and insights provided by Dr. Thomas McElroy and Dr. Sourav Sarakar during software complications.

Special thanks go to Andreas Gaertner for sharing and collaborating with me on the data gathered from STRAW. I would also like to extend my appreciation to the P-ONE Collaboration for their collaborative efforts and the work we accomplished together. I am also grateful to the University of Alberta for providing the resources that made this thesis possible.

On a personal note, I want to thank my parents and relatives—Susana Trejo, Juan José Miró, Tita y Chacho—for their endless and unconditional love and support, which enabled me to achieve the fulfillment of this thesis. A heartfelt thank you goes to my girlfriend, Fernanda Breña, who became my wonder wall when I needed it the most, enduring not only the rough times but also the distance. Finally, I extend my gratitude to Abraham, Alex, Karl, and Dima, who turned out to be a second family to me, never letting me feel lonely for one second.

Esta va por Pierre.

Table of Contents

1	Introduction	1
2	Background Theory	3
2.1	The Standard Model	3
2.1.1	Neutrino Discovery	4
2.2	Neutrino Properties	6
2.2.1	Neutrino Oscillation	6
2.2.2	Neutrino Mass	8
2.2.3	Neutrino Mixing Angles	9
2.3	Neutrino Interactions	10
2.4	Neutrino Flux	11
2.4.1	Astrophysical Neutrino Flux	13
2.5	Neutrino Detection	14
2.5.1	Cherenkov Light	14
2.5.2	Cherenkov Effect	15
2.5.3	Light Propagation	16
3	The Pacific Ocean Neutrino Experiment	18
3.1	Ocean Networks Canada	19
3.2	P-ONE Design	19
3.2.1	Detector Readout	23
3.3	STRAW	26
3.3.1	Attenuation Length	28
3.3.2	Potassium-40 Decay	30
3.3.3	Bioluminescence	31
3.4	Detection of Muon Tracks and Cascades	34
3.4.1	Muon Tracks	35
3.4.2	Cascades	37
3.5	Neutrino Telescopes	37

3.5.1	IceCube	37
3.5.2	Km3Net	38
3.5.3	Baikal-GVD	38
4	Simulation	40
4.1	IceTray	40
4.2	Muon Neutrino Flux	41
4.3	Monoenergetic Muons	46
4.4	Muon Neutrino Full Energy Spectrum	46
4.5	Cascade Simulation Full Energy Spectrum	47
4.6	Optical Module Response	47
5	Trigger Algorithm	49
5.1	Noise Rate Trigger	49
5.2	DOM Trigger	53
5.3	Selection of Reconstructable Events	55
5.4	String Spacing Optimization	56
5.5	Mono-Energetic Muon Efficiency	58
5.5.1	PMT Rate Cutoff	58
5.5.2	Adaptive Trigger	61
5.5.3	True Efficiency	64
5.6	Efficiency vs. Neutrino Energies	67
5.6.1	Muon Neutrino Efficiency	67
5.6.2	Electron Neutrino Efficiency	69
5.6.3	Tau Neutrino Efficiency	70
6	Conclusions	73
	Bibliography	76
	Appendix A: Simulation Output	82

List of Tables

3.1	Data size for every coincidence trigger.	24
3.2	Results of the measured attenuation length compared to the Geant4 cross-check for different wavelengths.[33]	29
3.3	Attenuation lengths from different neutrino experiment locations: Baikal-GVD, km3Net, IceCube and STRAW respectively.	29
5.1	Example of a list of 10ns window sets sorted by time for a DOM. . .	54

List of Figures

2.1	Table of The Standard Model of Particle Physics.	5
2.2	Neutral Current and Charged Current neutrino interactions.	11
2.3	Cosmic Neutrino flux schematic (2012) with respect of energy from different neutrino sources.	12
2.4	Representative example of various neutrino sources across decades of energy.	13
2.5	Sound wave emission schematic.	16
3.1	Diagram of the Ocean Networks Canada Western Infrastructure for monitoring the Pacific Ocean.	20
3.2	Diagram of the Cascadia Basin.	20
3.3	Proposed ten-string detector for P-ONE.	21
3.4	Proposed full detector for P-ONE.	22
3.5	Digital Optical Module (DOM) design for the P-ONE experiment.	22
3.6	Schematic of the two mooring lines from the STRAW mission.	27
3.7	Gaussian fits to coincident detection rate distributions of STRAW data.	31
3.8	Distribution of the levels of PMT coincidences in an Optical Module and the total rate from ^{40}K	32
3.9	Rate of a single photomultiplier over two minutes, measured in 30ms intervals.	33
3.10	Distribution of a single PMT background rates measured over two years of STRAW.	34
3.11	Illustration of a cascade, a track, and a double bang recorded in the IceCube Observatory.	35
3.12	Energy loss of muons for different materials.	36
4.1	Illustrative process of a simulation.	42
4.2	Energy distribution of sample events.	45

5.1	Average single DOM rate vs. PMT rate for different PMT coincidences in a DOM.	52
5.2	Number of events seen per year for 10TeV-10PeV muons weighted to an Astrophysical flux of a single power law and an Atmospheric flux.	57
5.3	Efficiency response depending on the maximum single DOM average rate permitted by limiting the rate on each individual DOM.	60
5.4	Fraction of time a certain n-PMT coincidence in a DOM is below the corresponding single DOM rate limit bin.	62
5.5	Efficiency response depending on the maximum single DOM average rate permitted by adapting the number of PMT hits required to trigger the DOM.	64
5.6	Fraction of time the detector rate is under the 8kHz limit when the DOM rate limit is set to 29Hz and 37Hz respectively.	65
5.7	Efficiency response when the detector rate is set to 29Hz and 37Hz respectively per DOM.	66
5.8	Muon neutrino efficiency at different energies.	68
5.9	Electron neutrino efficiency at different energies.	70
5.10	Tau neutrino efficiency at different energies.	71
A.1	Example of simulated events as seen through the Dataio-Shovel interface.	83
A.2	MMCTrackList key of a simulated muon.	84
A.3	I3MCTree key of a simulated muon.	85
A.4	The I3Photons key contains a list of all photons.	86
A.5	The trigger pulse map key contains the list of PMT hits on each DOM and on every string.	87

Chapter 1

Introduction

Neutrinos are considered an ideal astrophysical messenger since they offer the opportunity to explore the universe up to its highest energy frontiers. After the discovery of an astrophysical neutrino flux by the IceCube Neutrino Observatory in 2013[1], the subsequent identification of a link between these neutrinos and a γ -ray emitting blazar in 2017[2], and the most recent discovery of a second neutrino source from the active galaxy NGC 1068 in 2022[3], a global initiative has been underway to enhance exposure to astrophysical neutrinos significantly.

Ocean Networks Canada (ONC), an oceanographic observatory, provides a novel opportunity for constructing a large-volume neutrino telescope. The Cascadia Basin, situated at a depth of 2660 meters and powered by ONC, has been chosen to host the Pacific Ocean Neutrino Experiment (P-ONE). P-ONE will be designed as a new telescope for TeV-PeV neutrinos. The work on this thesis delves into the initial strategy for triggering the P-ONE detector.

Neutrinos, due to their neutral charge nature and interaction solely through the weak force, offer a distinctive avenue to investigate cosmic phenomena inaccessible to photons due to limited penetration depth, energy, or absorption along their journey to Earth. With neutrinos, it becomes possible to explore particle acceleration from extragalactic sources and particle interactions above the PeV scale. In addition to serving as a complementary astrophysical messenger to photons and providing a

baseline for neutrino oscillation studies, high-energy neutrinos hold the potential to unveil the identity and nature of dark matter.

The P-ONE detector site will be deployed underwater instead from in ice, because water has a larger scattering length than ice at 450m wave lengths desired for Cherenkov radiation detection, allowing for better neutrino timing reconstruction. (See section 2.5) Despite the higher background rate found in Cascadia Basin, (see section 3.3.3), which makes the triggering mechanism harder, the benefits of having a multi-km large detector, and a longer scattering length in water than ice, allows for the success of the experiment. (See section 3)

Trigger algorithms play a pivotal role in distinguishing relevant signals from background. The objective of this thesis is to maximise the trigger efficiency for all flavours while maintaining the detector limitations. There are two main sources of background in the P-ONE site. The first one is given by potassium-40 decays in the water and the second one is the presence of many living organisms capable of emitting bioluminescence. Moreover, the current bandwidth availability for triggering the detector represents a limiting factor of how much information the detector can process. The necessity of an optimal trigger strategy is imperative to be able to maximise the efficiency on detecting high-energy neutrino events despite the high rates of background.

The analysis was conducted through simulation and with the results obtained by P-ONE's first pathfinder after two years of data collection in the region. The latter provided the baseline to develop a bioluminescence model, that allowed for the estimation of trigger rates in the detector. The developed trigger algorithms accounted for the effects of the bioluminescence model in the efficiency, and the selected triggers were tested on each neutrino flavour at different energies.

Chapter 2

Background Theory

2.1 The Standard Model

The Standard Model of particle physics represents a triumph of human intellect and collaboration, offering a comprehensive framework for understanding the fundamental particles and forces that govern the universe. Over several decades, it has successfully accounted for a wide array of phenomena, like electromagnetism, the weak nuclear force and the strong nuclear force, and has provided predictions verified through experimental data.

The journey toward the establishment of the Standard Model began with the unification of the electromagnetic and weak nuclear forces by Sheldon Glashow, Abdus Salam, and Steven Weinberg in the 1970s,[4] which laid the foundation for the electroweak theory. This theoretical breakthrough addressed a question regarding the fundamental forces in the universe, but it also predicted the existence of massive, electrically neutral particles known as the W and Z bosons.

Figure 2.1 shows the table of the Standard Model of particle physics. It is divided into three main groups:

Quarks: Elementary particles and fundamental constituents of matter. They possess fractional electric charges and are never found in isolation, due to the strong force, which binds them together, with the exception of the top quark that decays faster than it forms a bound state. The combination of up and down quarks form the

atoms nuclei: protons and neutrons.

Leptons: Elementary particles that do not interact via the strong force. They can possess negative electric charge and fractional spin, defined as $\frac{1}{2}$, such as the electron, muon and tau. Neutrinos are also part of the lepton group, but they have neutral charge and can only interact via the weak force.

Bosons: They gauge bosons (spin-1) mediate the fundamental forces in the universe. The photon (mediator of electromagnetic force), W and Z bosons (mediators of weak nuclear force), and the gluon (mediator of the strong nuclear force). Lastly, the Higgs boson that is responsible for giving mass to other fundamental particles through the Higgs mechanism.

2.1.1 Neutrino Discovery

The quest to detect neutrinos commenced in 1930 when a problem had arisen in the study of nuclear beta decay. We now know that beta decay is the process where an unstable atom radioactively decays into a more stable one while producing an electron (positron) and a neutrino, but at the time it was only believed that the decay only produced an electron. However, experiments showed that the conservation of energy was not preserved in the reaction. Pauli was the first to suggest that the "missing" energy was in fact another particle emitted along with the electron, that he named: *neutron*. In 1933 Fermi presented the theory of beta decay where Pauli's particle was incorporated with the quality that it needed to be extremely light. The first direct evidence of their existence was furnished by the Cowan-Reines experiment in 1956.[6] This experiment successfully detected antineutrinos emitted by nuclear reactors through their interactions with protons, providing empirical support for a new family of particles.

Neutrinos, categorized into three flavours (electron, muon, and tau), are characterized by their exceptionally weak interactions with matter at low energies. This elusive nature earned them the nickname "ghost particles." The successful detection

Standard Model of Elementary Particles

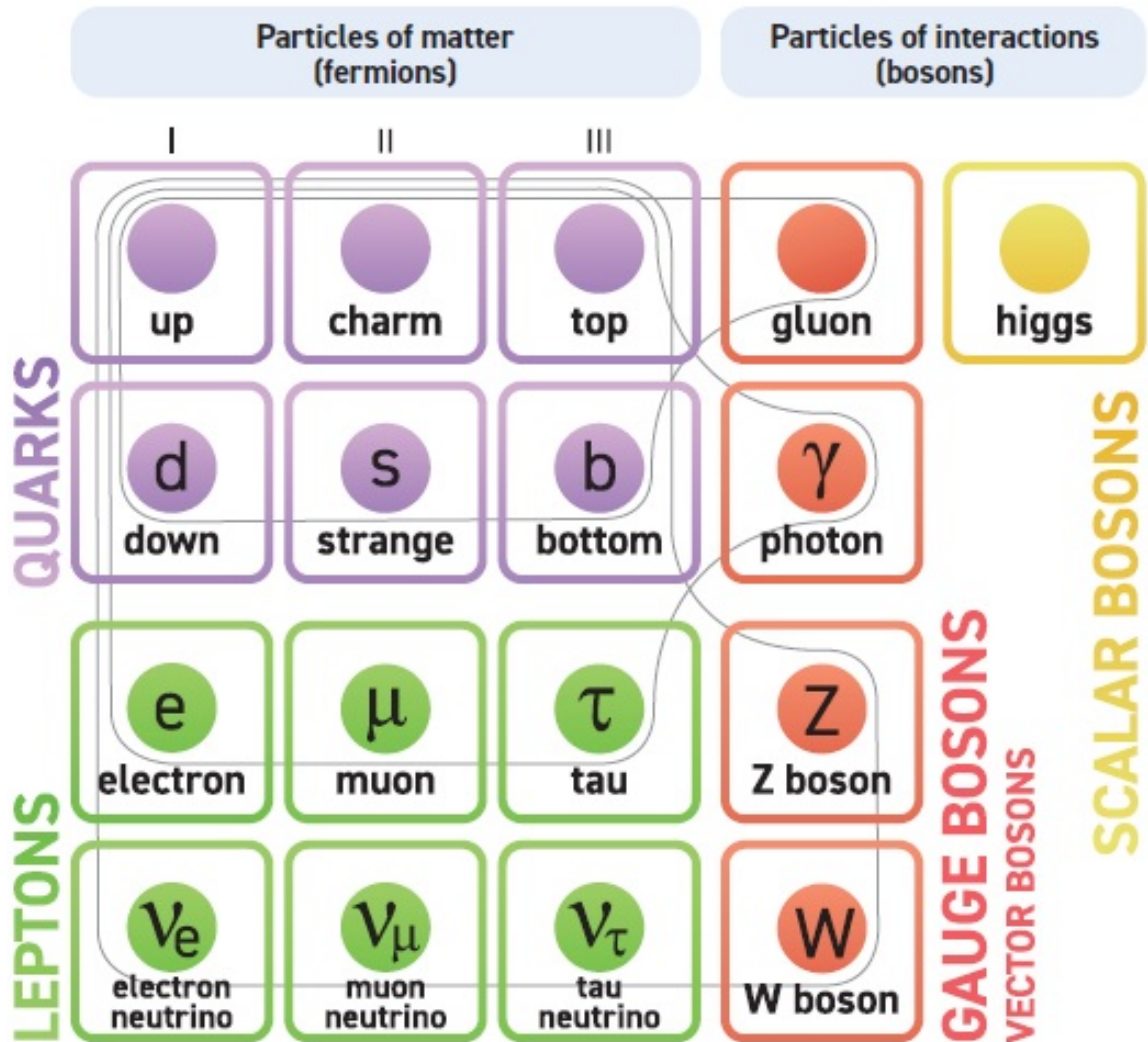


Figure 2.1: Table of The Standard Model of Particle Physics [5]. It is divided into three main groups: quarks, leptons and bosons.

of neutrinos represented a momentous achievement in particle physics by confirming Pauli's prediction of the existence of a very light neutral particle that Fermi eventually called: *neutrino* [7].

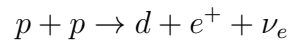
2.2 Neutrino Properties

Neutrinos are elusive particles with unique properties that make them intriguing subjects of study in the field of particle physics. In this section, we explore their known properties, which play a critical role in their detection.

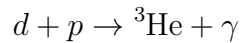
2.2.1 Neutrino Oscillation

With the discovery of the neutrino, a new approach to understand the nuclear effects happening at the centre of the Sun was possible. Since 1938, the pp chain process, was the one followed to describe the fusion nuclear processes in the Sun's core. This process consisted of the following [8]:

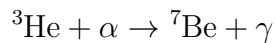
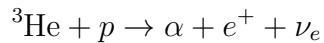
- Two protons make a deuteron:



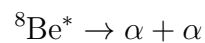
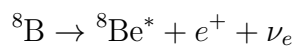
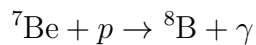
- Deuteron plus proton makes ${}^3\text{He}$:



- Helium-3 makes alpha particles or ${}^7\text{Be}$:

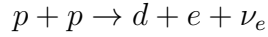


- Beryllium makes alpha particles:

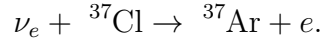


The alpha particles from this interaction can take thousands of years to get from the centre to the surface of the Sun, hindering drawing any significant conclusions on its nature.

On the other hand, the initial reaction,



emit neutrinos that can travel through the surface without interacting with any other nuclei, making it possible to study the initial reaction of the nuclear fusion process in the Sun. In 1968, Davis *et al.*[9] reported the first detection of solar neutrinos by using a tank of cleaning fluid which contained Chlorine, so the neutrino gets absorbed by the element and converted to Argon in the reaction. Essentially:



The number of neutrinos detected was less than half of the one predicted. Thus was born the *solar neutrino problem*.

In 1968, Pontecorvo proposed that the neutrino produced by the sun is transforming in flight into a different flavour. This mechanism is now what we call *neutrino oscillation*. [8] Simply explained, it is the quantum mechanics of mixed states. Considering only ν_μ and ν_e , the stationary states of a neutrino is the orthogonal linear combination of both, as equation 2.1 shows.

$$\nu_1 = \cos \theta \nu_\mu - \sin \theta \nu_e; \quad \nu_2 = \sin \theta \nu_\mu + \cos \theta \nu_e \quad (2.1)$$

After adding time dependence to each neutrino: $e^{-\frac{iE_1 t}{\hbar}}$, and solving for ν_μ from equation 2.1, it is possible to obtain the probability of transitioning between flavours as a function of time, like equation 2.2 shows.

$$P_{\nu_e \rightarrow \nu_\mu} = \left[\sin(2\theta) \sin \left(\frac{(m_2^2 - m_1^2)c^4}{4\hbar E} t \right) \right]^2 \quad (2.2)$$

From function 2.2 it is now evident that the probability of being at any flavour state follows a sinusoidal function, meaning that a neutrino can *oscillate* across all flavours. In order to find the maximum probability of oscillation then, after a particular distance:

$$L = \frac{2\pi\hbar E}{(m_2^2 - m_1^2)c^3},$$

the probability of conversion hits a maximum. This is telling us that for this phenomenon to happen, the Δm^2 term should be different than zero, suggesting that neutrinos have a non-zero mass.

Notice that there is a requirement of a mixing angle θ and the masses must be unequal and greater than zero, for oscillations to occur. This will be covered later in section 2.2.3.

In 2001, the Super-Kamiokande collaboration and the Sudbury Neutrino Observatory (SNO) collaboration, confirmed the theory of neutrino oscillations. The SNO experiment used heavy water (D_2O) and solar neutrinos. The virtue of heavy water is that the neutrons present allow for detection of both electron neutrinos and the total neutrino flux.[10] Comparatively, Super-Kamiokande used ordinary water, and a larger detector size, that increased the statistics of the detection of electron neutrinos, because their detection method focused on the elastic neutrino-electron scattering.[11] Both experiments showed consistency on their measurements and in 2002 [12], SNO published the result that solved to the solar neutrino problem showing that:

$$\theta_{sol} \approx \frac{\pi}{6}, \quad \Delta(m_{sol}^2) \approx 8 \times 10^{-5} (\text{eV}/c^2)^2$$

2.2.2 Neutrino Mass

Since there are three known neutrino flavours, there are three mass splittings: Δm_{21} , Δm_{31} and Δm_{32} . Unfortunately, with neutrino oscillations it is only possible to determine the difference between the masses squared, but not the actual mass of the particle. It has been already measured a small difference between m_1 and m_2

($\Delta m_{21}^2 \sim 0.0001 \text{ (eV/c}^2)^2$), but a larger difference to m_3 ($\Delta m_{32}^2 \sim 0.003 \text{ (eV/c}^2)^2$).[8] This has two possible interpretations, either the lightest is the first generation, like the quark and lepton masses, and the heaviest is the third, meaning that $m_3 > m_2 > m_1$, or that there is an inverted mass hierarchy on neutrinos: $m_2 > m_1 > m_3$.

Currently the only direct mass measurements have so far only put an upper bound limit on the mass. This is done by looking at the beta-decay spectrum of tritium [13]. The tritium molecule is an example of an unstable radioactive atom whose decay is composed by a ${}^3\text{HeT}^+$ molecule, an electron and an electron neutrino.

The KATRIN collaboration published an upper bound limit of $m_\nu < 0.8\text{eV}/c^2$ using this method.[14]

2.2.3 Neutrino Mixing Angles

The mixing state of a neutrino is composed by the three neutrino flavours and their mixing angle. The Pontecorvo–Maki–Nakagawa–Sakata (PMNS) matrix relates the neutrino eigenstates with the neutrino flavours as seen in equation 2.3, where U can be expressed in terms of the three angles θ_{12} , θ_{13} and θ_{23} and a complex phase factor (δ). Equation 2.4 shows the U matrix, where $c_{ij} = \cos \theta_{ij}$ and $s_{ij} = \sin \theta_{ij}$.

$$\begin{pmatrix} \nu_e \\ \nu_\mu \\ \nu_\tau \end{pmatrix} = \begin{pmatrix} U_{e1} & U_{e2} & U_{e3} \\ U_{\mu1} & U_{\mu2} & U_{\mu3} \\ U_{\tau1} & U_{\tau2} & U_{\tau3} \end{pmatrix} \begin{pmatrix} \nu_1 \\ \nu_2 \\ \nu_3 \end{pmatrix} \quad (2.3)$$

$$U = \begin{pmatrix} c_{12}c_{13} & s_{12}c_{13} & s_{13}e^{-i\delta} \\ -s_{12}c_{23} - c_{12}s_{23}s_{13}e^{i\delta} & c_{12}c_{23} - s_{12}s_{23}s_{13}e^{i\delta} & s_{23}c_{13} \\ s_{12}s_{23} - c_{12}c_{23}s_{13}e^{i\delta} & -c_{12}s_{23} - s_{12}c_{23}s_{13}e^{i\delta} & c_{23}c_{13} \end{pmatrix} \quad (2.4)$$

The neutrino mixing angle matrix is not diagonal, unlike the quark mixing angle matrix which is mostly diagonal. Two of the leptonic mixing angles are known to be large $\theta_{12} \approx \theta_{sol} = 34 \pm 2^\circ$ and $\theta_{23} \approx \theta_{atm} = 45 \pm 8^\circ$. On the other hand θ_{13} is known to be less than 10° .

2.3 Neutrino Interactions

Neutrino interactions with matter are essential for their detection. Neutrinos only interact via weak interactions, making them difficult to capture. Two types of neutrino interactions are prominent:

Charged-Current (CC) Interactions: In CC interactions, a neutrino interacts by exchanging a W boson with a target nucleus or electron. These interactions are crucial for studying the neutrino's flavour-changing properties. In equation 2.5 it is shown how when a neutrino from any flavour ν_l interacts with a nucleon N , the product of the interaction are the charged lepton from the corresponding neutrino flavour l plus a hadronic shower of particles X .

$$CC : \quad \nu_l + N \rightarrow l + X \quad (2.5)$$

Figure 2.2 shows a Feynman diagram of a charged current interaction between a neutrino and a quark via a W boson. The product is a lepton and a quark with a different flavour.

Neutral-Current (NC) Interactions: In NC interactions, a neutrino interacts via the exchange of a Z boson. These interactions are sensitive to the weak neutral current and are vital for understanding neutrino properties. In equation 2.6 it is shown how when a neutrino from any flavour ν interacts with a nucleon, the interaction product of a NC interaction are the neutrino from the same flavour ν plus a hadronic shower X if enough energy is transferred to the nucleus.

$$NC : \quad \nu_l + N \rightarrow \nu_l + X \quad (2.6)$$

Figure 2.2 shows a Feynman diagram of a NC interaction between a neutrino and a quark via a Z boson. Contrary to the CC case, the product is a neutrino and a quark.

Neutrino cross sections are measures of the likelihood of neutrino interactions with

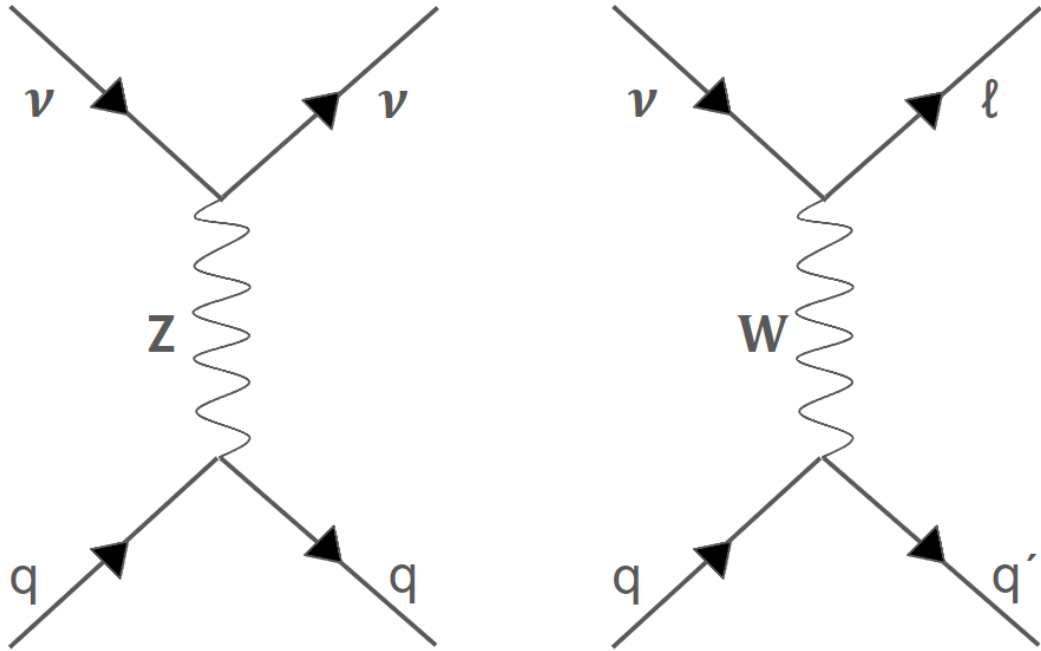


Figure 2.2: Neutral Current neutrino interaction of a neutrino interacting with a quark via Z boson, resulting in a neutrino and quark product. (Left) Charged Current neutrino interaction of a neutrino interacting with a quark via W boson resulting in a lepton and quark product. (Right)

matter. They depend on the neutrino energy, the type of interaction, and the target material.

Understanding neutrino interactions and cross sections is pivotal for designing experiments that aim to detect and study neutrinos, from solar and atmospheric neutrinos to neutrinos produced in particle accelerators and nuclear reactors.

2.4 Neutrino Flux

Understanding neutrino fluxes, the flow of neutrinos per unit area, is important in order to be able to calculate the expected event rates. These fluxes are highly dependent on the source of neutrinos, whether they originate from astrophysical sources like supernovae, the Sun, or cosmic rays interacting with Earth's atmosphere. The discovery of the astrophysical flux was made by IceCube in 2013[1], where they observed a high-energy neutrino flux from extrasolar sources, offering a new way to look

into the universe.

Figure 2.3 shows a schematic of all the known neutrino fluxes from different neutrinos sources. Despite the predicted flux of cosmological neutrinos, which are the neutrinos remaining from the Big Bang, their small energies make them impossible to detect with our current technology. On the other side of the spectrum, the Cosmogenic neutrinos are those who are emitted by an extra-galactic cosmic ray source. There has not been a detection of a Cosmogenic neutrinos yet.

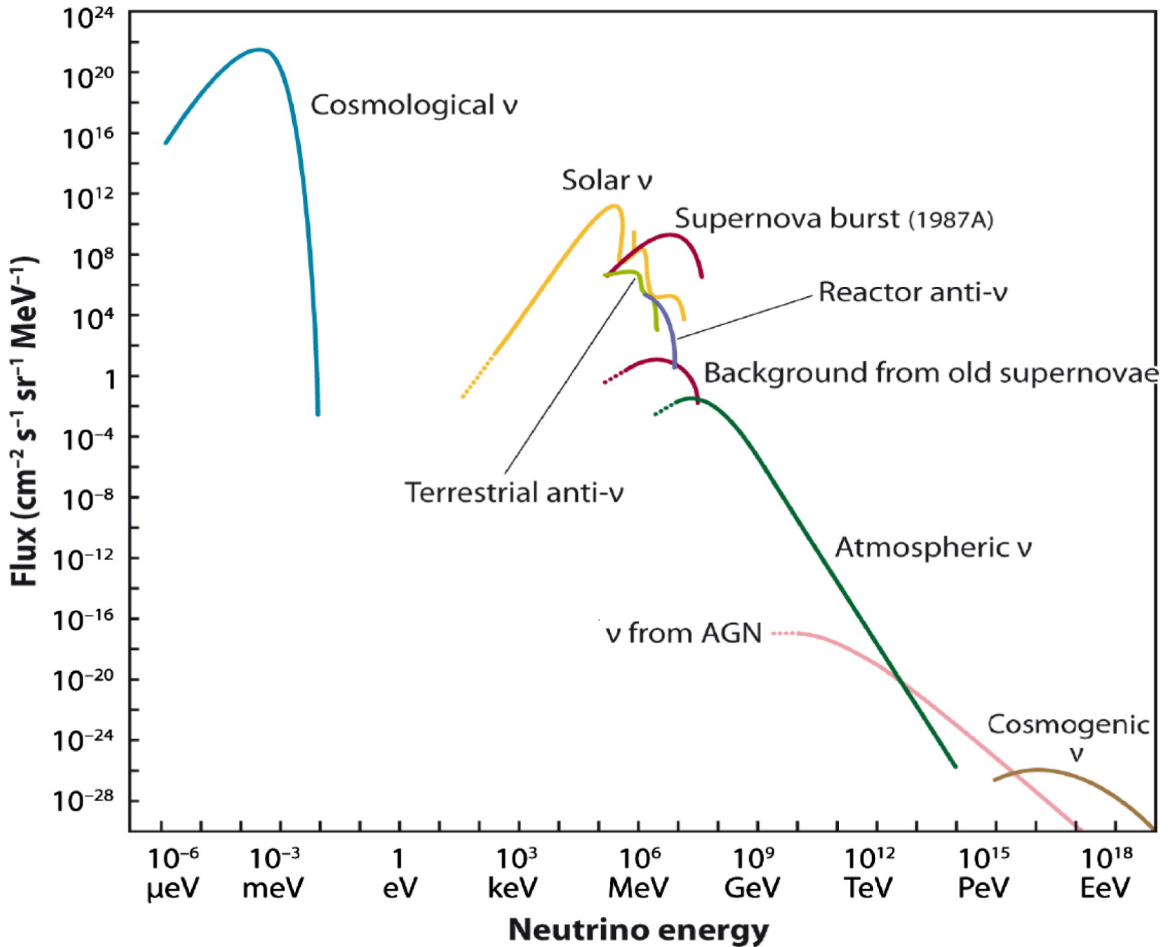


Figure 2.3: Cosmic Neutrino flux schematic (2012) with respect of energy from different neutrino sources. At low energies we find cosmological neutrinos which are the neutrinos remaining from the Big Bang. Despite their high flux, their low energies makes them impossible to detect with out current technologies. On the other side of the spectrum, the Cosmogenic neutrinos are those who are emitted by an extra-galactic cosmic ray source. The Cosmogenic neutrinos are yet to be detected.[15]

For a better comparison, figure 2.4 shows a representation of the neutrino cross

section vs. the neutrino energy. It is clear that low energy neutrinos, like the cosmological flux, have the smallest cross section, making its detection impossible with the current neutrino detectors. At the same time, as the energy increases, their cross sections do too, but the flux decreases. The increased cross-section is beneficial for the detection of neutrinos because it means a larger amounts of light emitted in the detector.

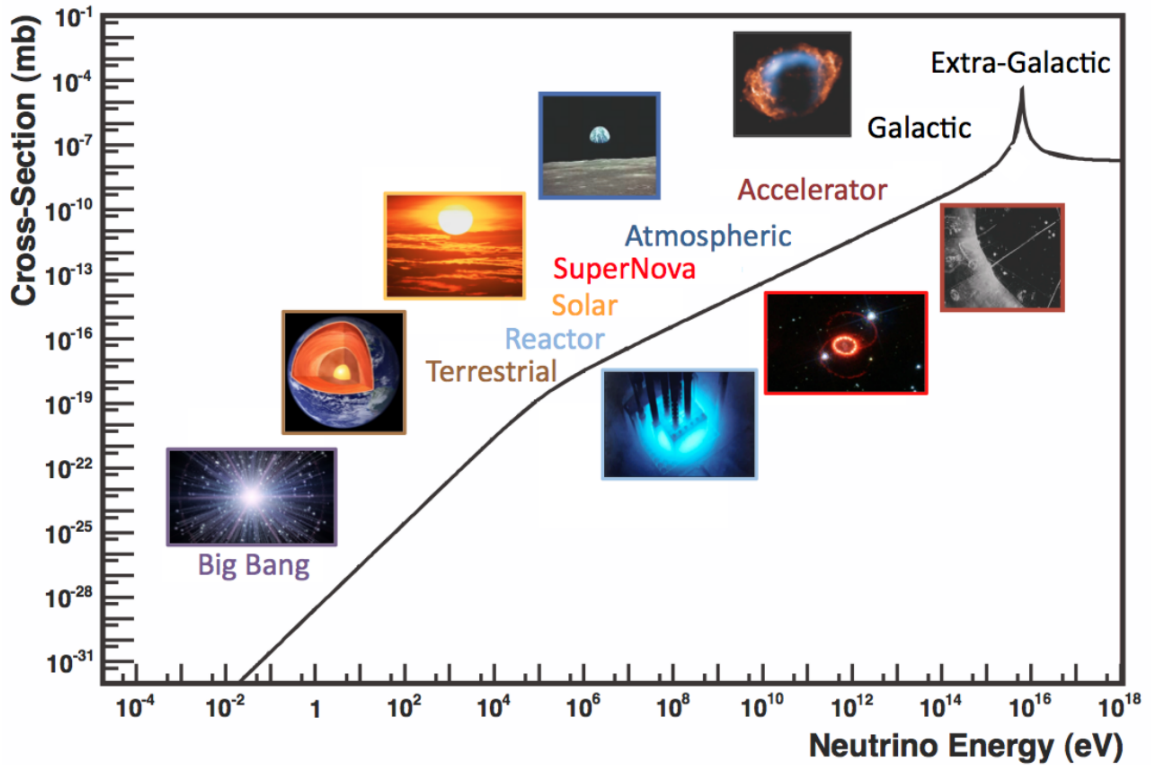


Figure 2.4: Representative example of various neutrino sources across decades of energy. The electroweak cross-section for the scattering on free electrons as a function of neutrino energy is shown for comparison. The peak at 10^{16} eV is due to the Glashow resonance, a phenomenon that only happens at really high energies and yields a distinct signature from all the previous ones. Beyond this energy, the cross section stops increasing with energy.[16]

2.4.1 Astrophysical Neutrino Flux

Astrophysical neutrinos, originating from distant astrophysical sources such as active galactic nuclei, possess properties that make them particularly appealing for the con-

struction of large neutrino detectors.[17] Their high energies allow them to traverse cosmic distances, making them messengers from the most extreme environments in the universe. Their ability to travel through vast cosmic distances without significant absorption in matter makes them valuable for studying astrophysical phenomena that produce them. Large neutrino telescopes like IceCube[18] and KM3NeT[19] are designed to observe these high-energy neutrinos and reveal the most energetic processes in the cosmos.

2.5 Neutrino Detection

Neutrino detection has proved to be a challenging process. Given how small neutrino cross section is, many new detection techniques have been developed in order to detect them. The multiple detection techniques designed as of today, depend highly on the source of neutrinos. For instance, solar neutrinos come with an abundant flux and the energy ranges from the keV – MeV. Low-energy neutrinos are best detected with a denser detector array *i.e.* Super Kamiokande and SNO[20, 21], than with a massive one *i.e.* the IceCube detector.[18] On the other hand astrophysical neutrinos have a heavily suppressed flux, but their energies can get up to the PeV range. Large, sparse neutrino detectors are consequently built to compensate the small cross section of the neutrino, as well as to cover a larger volume that allows a larger exposition to smaller fluxes, like the astrophysical flux. Detecting neutrinos usually involves observing either the muon produced in the interaction, the hadronic part of an interaction and/or if a charged interaction occurs, the observation of a charged lepton depending on the flavour of the neutrino.

2.5.1 Cherenkov Light

The fundamental working principle of water/ice neutrino detectors lies in the detection of Cherenkov light from charged secondary particles created in neutrino interactions with the detector medium.

During CC neutrino interactions, most of the energy is carried away by the lepton, with the rest of the energy deposited in hadronic or electro- magnetic particle showers [22]. These showers produce Cherenkov light that can be detected by photodetectors.

2.5.2 Cherenkov Effect

When a charged particle moves through a material, it induces a polarization of the surrounding matter. If the particle exceeds the speed of light in that material, the wave patterns form a cone around the particle, leading to the emission of light that is perpendicular to this cone. This phenomenon is commonly referred to as the Cherenkov effect. [23]

The Cherenkov cone is similar to the one created when an object travels faster than the speed of sound; a sonic boom. Figure 2.5 shows on the left an illustration of the sound waves emitted by an object as it propagates through space, it is the regular Doppler effect. In contrast, at the right there is displayed an illustration of an object emitting sound waves but it is moving faster than the speed of sound. Since the source is traveling faster than the waves, the waves never catch up to the source, hence creating this particular cone.

Given a material refractive index n , the speed of light in that medium will be given by $c_n = \frac{c_0}{n}$. From this, the angle of light emitted by a particle travelling at speed v , is calculated with:

$$\cos \theta = \frac{c_0}{v \cdot n}$$

Considering water has a refractive index of $n \approx 1.3$, for a highly relativistic particle, $c_0/v \approx 1$, the Cherenkov angle is around 41° .

The number of emitted Cherenkov photons is given by Frank-Tahmm formula[24] shown in equation 2.7. N , the number of photons, depends mostly on λ ; the wavelength, and x ; the distance traveled by the particle. Naturally this phenomenon also depends on the fine structure α of the medium and the charge of the particle z . In

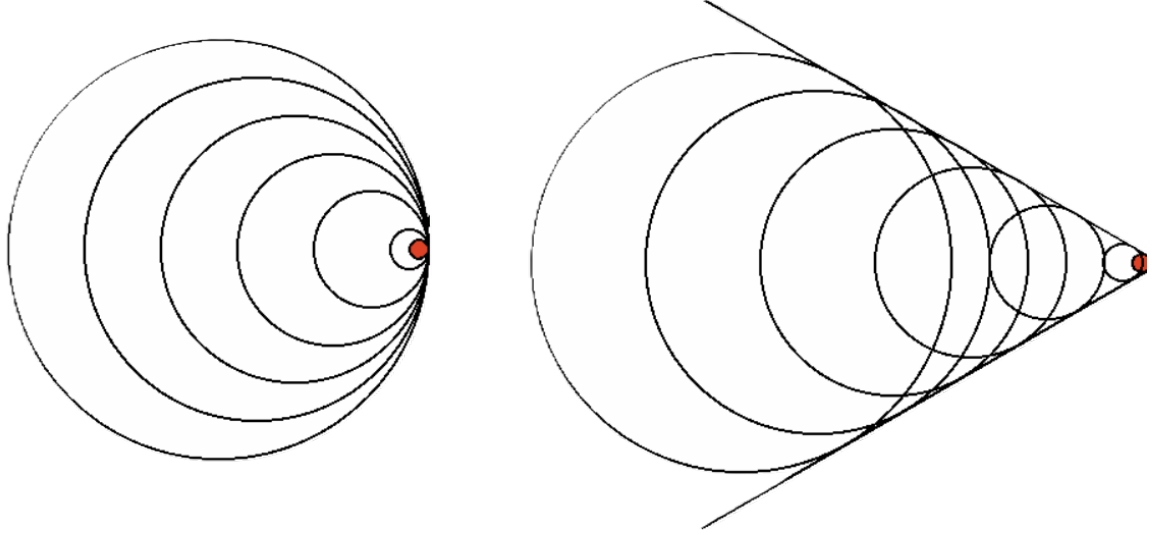


Figure 2.5: Object emitting sound waves propagating through space. (left) Object moving faster than the speed of sound. It does not allow the sound waves to catch up to the source creating a sonic boom cone.(right)

water and ice, the typical wavelength spectrum is constrained from 300nm to 600nm with around 3×10^4 photons emitted per metre. [25]

$$\frac{dN}{d\lambda dx} = \frac{2\pi\alpha z^2}{\lambda^2} \cdot \left(1 - \frac{1}{\beta^2 n^2(\lambda)}\right) = \frac{2\pi\alpha z^2}{\lambda^2} \cdot \sin^2(\Theta) \quad (2.7)$$

2.5.3 Light Propagation

In water light undergoes two types of physical interactions: scattering changes the direction of the photon, and absorption when the photon is lost inside the water molecule. The combination of both is called light attenuation and can be obtained by adding the inverse of both scattering and absorption lengths as equation 2.8 shows, where L_a is the absorption length and L_s is the scattered length.

$$L_{\text{att}} = \left(\frac{1}{L_a} + \frac{1}{L_s}\right)^{-1} \quad (2.8)$$

The two most common ways to quantify either the absorption length and the scattering length of the photon is with the following parameters[26]:

- The absorption length $L_a(\lambda)$, with λ being the wavelength of the photon. It

describes the exponential decrease of non-absorbed photons as a function of distance. As shown in equation 2.9.

$$N = N_0 \cdot e^{\frac{-r}{L_a}} \quad (2.9)$$

- The scattering length $L_s(\lambda)$, and it is defined as the exponential decrease of the number N of non-scattered photons as a function of distance.

$$N = N_0 \cdot e^{\frac{-r}{L_s}} \quad (2.10)$$

- The effective scattering length (L_{eff}), defined in equation 2.11, that depends on the geometrical scattering length and the mean cosine of the scattering angle θ . L_{eff} is a "normalization" of the scattered length for different scattering angle distributions to one with $\langle \cos(\theta) \rangle = 0$. [27]

$$L_{\text{eff}} = \frac{L_s}{(1 - \langle \cos(\theta) \rangle)} \quad (2.11)$$

Chapter 3

The Pacific Ocean Neutrino Experiment

The Pacific Ocean Neutrino Experiment (P-ONE)[28] is a new initiative with a vision of constructing a multi-cubic kilometre neutrino telescope, to expand our observable window of the universe at higher energies and study high energy interactions. It will be installed 2km deep underwater in the Cascadia Basin off the west coast of the Vancouver Island in British Columbia, Canada, using the infrastructure provided by Ocean Networks Canada.[29]

Following IceCube's discovery of an astrophysical flux of neutrinos in 2013,[1, 30] and the following link between these neutrinos and γ -ray emitting blazar in 2017,[2] an international effort has started to improve the integral exposure to astrophysical neutrinos that would provide insights of the processes happening inside active-galactic nuclei. Ocean Networks Canada (ONC), an oceanographic observatory, offered a new opportunity for the construction of a large neutrino detector. P-ONE, as a new detector for TeV-PeV neutrinos will be built using a modular deployment approach.

With neutrinos as astrophysical messengers, the physics of particle acceleration, particle interaction above PeV, and other neutrino interactions under extreme energy conditions can be explored with P-ONE.[31]

As already demonstrated by IceCube [1], in order to achieve high sensitivity to astrophysical neutrinos, a volume of a cubic-kilometre or higher detector is needed.

The ground breaking discovery of observing an isotropic astrophysical neutrino flux at the TeV-PeV scale, suggests the existence of an unknown class of extra galactic astrophysical objects that are accelerating protons to at least $10^{16} - 10^{18}$ eV. P-ONE will aim to look into the remaining areas of space that has not been looked into by IceCube.[29] In addition to this, water has a longer scattering length than ice, and a shorter absorption length, allowing for a better timing resolution for the reconstruction of some events, i.e. tau reconstruction, due to their double bang signature that characterizes them. This will be reviewed later in section 3.4.

3.1 Ocean Networks Canada

The construction and implementation of P-ONE is supported by Ocean Networks Canada (ONC), an oceanography observatory with over 800km of an underwater-cabled network monitoring the west and east coasts of Canada. ONC uses cabled observatories, remote control systems and interactive sensors that would provide insights on deep ocean observing, natural hazards and ocean soundscapes.[32]

Figure 3.1 shows the 800km NEPTUNE observatory and the 50km VENUS observatory. NEPTUNE will become the hosting network for P-ONE. The node is located in the Cascadia Basin, which is a heavily sedimented abyssal plain located 2660m below the sea level. See figure 3.2. [32]

Its characteristic environment consists of below 2°C temperatures, pressures of 300atm, and complete absence of light from the sun. Despite the extreme conditions there are a large variety of organisms that have adapted to such conditions and which live in the region.

3.2 P-ONE Design

The first stage of P-ONE will consist on 10 string segments that are to be deployed deep underwater in the NEPTUNE observatory in Cascadia Basin at approximately



Figure 3.1: A diagram of the Ocean Networks Canada Western Infrastructure for monitoring the Pacific Ocean. This contains the NEPTUNE and VENUS observatories. Source: [32]

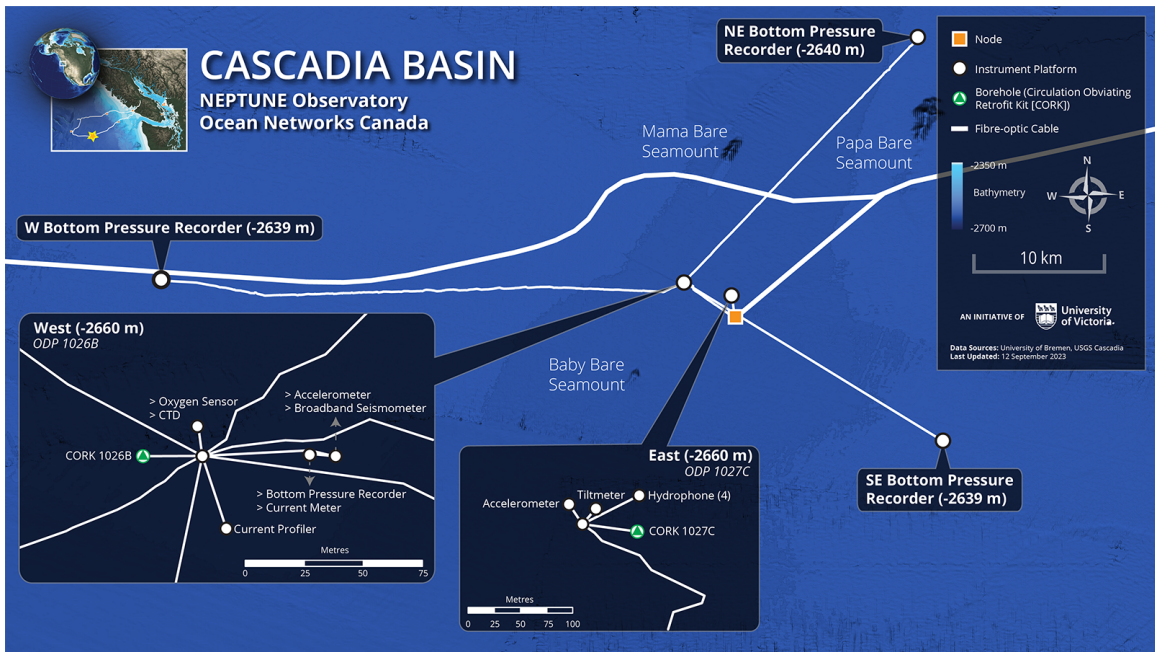


Figure 3.2: Diagram of the Cascadia Basin, the site where P-ONE will be installed, and former site of STRAW and STRAW-b pathfinders. Source: [32]

2600m. Each string will consist of 20 Digital Optical Modules (DOMs), where at least two of which will be calibration modules. There is a 50m separation between

DOMs on the string, starting at 50m from the ocean floor, adding up to a 1050m long detector line. See figure 3.3.

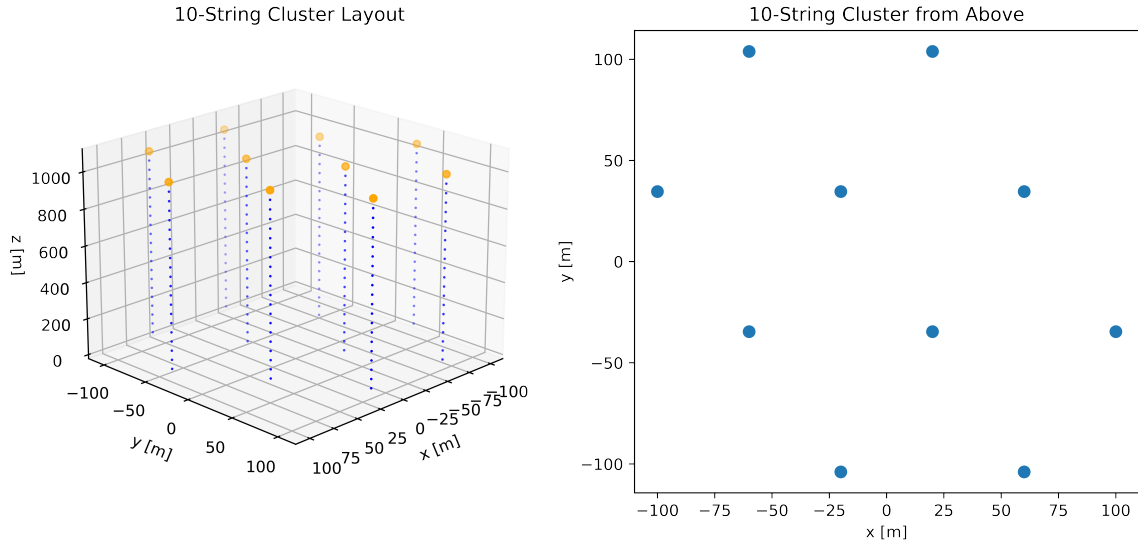


Figure 3.3: Proposed ten-string detector for P-ONE. Left: 3D projection of the 20 DOMs string with the buoy on top. Right: Geometry of the selected string array as seen from above. The separation distance between strings is 80m.(not-scaled)

In order to cover a larger volume, a detector consisting of 7 ten-string cluster is proposed; strategically arranged to best detect muon tracks and cascade events. See section 3.4. Figure 3.4 shows the initial proposal of the geometry of the full 70-string detector and the geometry of the 10-string cluster.

The first ten-string cluster will be an hexagonal array of strings with a separation distance of 80m between strings. In section 5.4 an exercise was conducted in order to find the most optimal string separation for the detector. At the bottom of each string there will be a mini Junction Box (mJB) that anchors to the ocean floor. The mJB of each string is connected to a Cluster Junction Box (CJB), that is connected to the node provided by ONC that brings the network to shore. In order to keep the strings vertical, a buoy will be added at the top of the mooring line so it keeps the string straight. Figure 3.3 shows the first cluster detector geometry, from a 3D perspective and from above.

Each DOM will consist on an arrangement of 16 PMTs, with 8 on each hemisphere

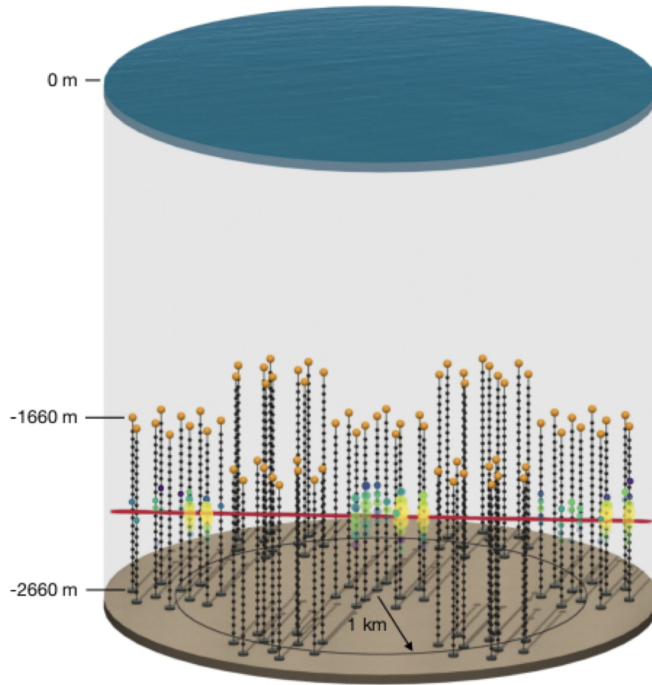


Figure 3.4: Proposed full detector for P-ONE. Displayed there is an example of a muon track going through the volume, hitting three separate clusters.[11]



Figure 3.5: Digital Optical Module (DOM) design for the P-ONE experiment. There is a total of 16 PMTs (showcased as the yellow elements) divided into two 8-PMTs hemispheres. Notice the titanium ring between both hemispheres. The cable that connects multiple DOMs in a string crosses the DOM in the centre, through the titanium ring.[28]

of the DOM. There will be a titanium ring separating both hemispheres, which is the dedicated space for cables. The string cables will come out directly from the top and bottom of the sphere. Figure 3.5 shows an illustration of a DOM.

3.2.1 Detector Readout

Each DOM, composed of 16 PMTs, is connected to its neighbouring DOM by a 10Mb copper ethernet link, this means that each DOM will only have 5Mb for triggering and readout. The string connection to the mJB is 1000Mb copper ethernet link. The cluster contains 10 strings connected to the CJB over a 1Gb link. The CJB to shore connection is 1Gb too.

The P-ONE detector has four distinct hardware levels relevant to the trigger system. Since there is the need, for multiple trigger algorithms at each of these stages we use the terminology of *Level* to denote them. The three key levels are:

L1: These triggers are generated by a single DOM and are typically based on a number of PMTs in the DOM.

L2: Triggers at this level are the result of an algorithm running at the detector level. This means that the whole detector looks for an event instead of triggering on every DOM. The triggers are sent out to all optical modules with a time window and cause every optical module to readout the corresponding waveform data to the shore. This provides a full-detector readout that allows for coincidences of multiple DOMs. This trigger is limited by the total readout bandwidth available from the detector to shore.

L3: This is the final trigger level and is designed to be implemented on-shore in a data centre where there will be sufficient resources to run an initial event reconstruction to further reduce the event rate before the data are stored. This level is limited by how much storage space we can afford.

The lowest level trigger is a coincidence of PMTs in a DOM. The trigger contains the time stamp and details of a PMT coincidence at the level of a DOM. For the purposes of this document we will assume that a 32-bit, 10ns timestamp is sufficient to resolve any timing ambiguities within the trigger and data acquisition. Along with the 32-bit time stamp, we assume that a 16-bit coincidence mask showing the hit PMTs in the DOM plus an additional 16-bits of information that may include time over threshold information will be sent making each trigger coincidence have a size of 8 bytes. See table 3.1.

Time Stamp	PMT hits in DOM	Event Features	Total
32-bit	16-bit	16-bit	8 bytes

Table 3.1: Data size for every coincidence trigger. Every trigger will include the time stamp, the number of PMT hits in a DOM and some relevant event features, like time over threshold.

For the data readout we assume that a 50ns portion of the PMT waveform will be read out, corresponding to 10 Analog-to-Digital-Converter (ADC) samples. Since the ADC data has a 12-bit resolution this means 15 bytes of ADC data to which we add 4 bytes of time stamp and 1 byte for the PMT number leading to a total of 20 bytes per PMT hit.

Triggering P-ONE will, as far as each DOM is concerned, be a two-stage process. Each DOM will send out a trigger packet based on local coincidences. Some central logic will collect these and decide whether to trigger a readout and, if a readout is triggered each DOM will receive a readout window and will readout all the PMT hits corresponding to that window.

The size of the DAQ window is $5\mu\text{s}$ and the average PMT noise rate is 50kHz, which is the median background rate measured in the region, (see section 3.3.3), for each of the 16 PMTs in every DOM. This means that we expect each DOM to have, on average, 4.0 hits per readout. We previously estimated the data size of each hit to be 20 bytes and so this means that for every event readout each DOM will be sending

80 bytes of data.

If the rate of coincidence triggers per DOM is r_c and the rate of event readout is r_r then the total bandwidth in bytes per second used per DOM is equation 3.1, where n_c is the number of bytes sent per coincidence and n_r is the number of bytes sent per readout.

$$B_{DOM} = n_c r_c + n_r r_r \quad (3.1)$$

Since we know the total bandwidth per DOM and have estimates for both data sizes in order to calculate the maximum rates we need to know how r_c and r_r are related. This depends on the trigger algorithm which receives the coincidence events and decides whether a full readout is warranted. To keep this simple we will assume that this algorithm will only look for coincidences in a DOM to trigger. In this case, the rate of readouts is given by equation 3.2, where r_r is 200 times the rate of coincidence trigger per DOM because the detector is composed by 200 DOMs. Substituting this into our expression for the bandwidth per DOM we get equation 3.3.

$$r_r = 200r_c \quad (3.2)$$

$$B_{DOM} = r_c [n_c + 200n_r] \quad (3.3)$$

For the case where we only trigger on one DOM; where we fire the readout for every DOM coincidence we get equation 3.4. Substituting the known variables, we get a single DOM coincidence rate of 39Hz, which corresponds to 7800Hz for the full cluster.

$$r_c = \frac{B_{DOM}}{n_c + 200n_r} \quad (3.4)$$

These results are very important because they represent the maximum rate the detector can handle before saturating the available bandwidth.

3.3 STRAW

In 2017 the STRings for Absorption length in Water (STRAW) mission was created. STRAW mission was the pathfinder whose goal was a systematic, step-by-step investigation of the *in-situ* optical transparency and ambient background light of the P-ONE site. The experiment took data underwater, at Cascadia Basin for 4 years combined, where they measured the optical properties of water, and provided initial estimates of bioluminescence, potassium-40 decays and deep-water biofouling.[33]

It consisted of two optical module lines, with 4 optical modules each. They were instrumented with light emitter modules and light receiving modules mounted at different heights from the seafloor. The light emitter module called Precision Optical Calibration Module (POCAM), provided an isotropic and 4-8ns pulse of light. The light receiving module, or STRAW Digital Optical Module (sDOM), consisted on two PMTs: one facing upwards, the second; downwards. The POCAM was equipped with a LED that flashed different wavelengths of light, and it was synchronized with the sDOMs in order to measure the attenuation length of the water. At the same time the sDOMs also monitored the background light produced by the radioactivity from the ^{40}K decay and bioluminescence. The first module was 30m above the sea floor, and the remaining 3 modules were spaced out such that the top module was at 110m from the sea floor. The precise details of module height, total string length and the 37 module separation is shown in figure 3.6.[34] By 2018 both lines were already taking data of the region where P-ONE will be installed. Figure 3.6 shows a diagram of the completed STRAW pathfinder.

The site proved to be ideal for a construction of a new neutrino detector, with weak ocean currents of 3 to 7 cm/s, stable temperatures of 2°C and pre-existing underwater infrastructure to power the detector and send the data acquired to shore.[35]

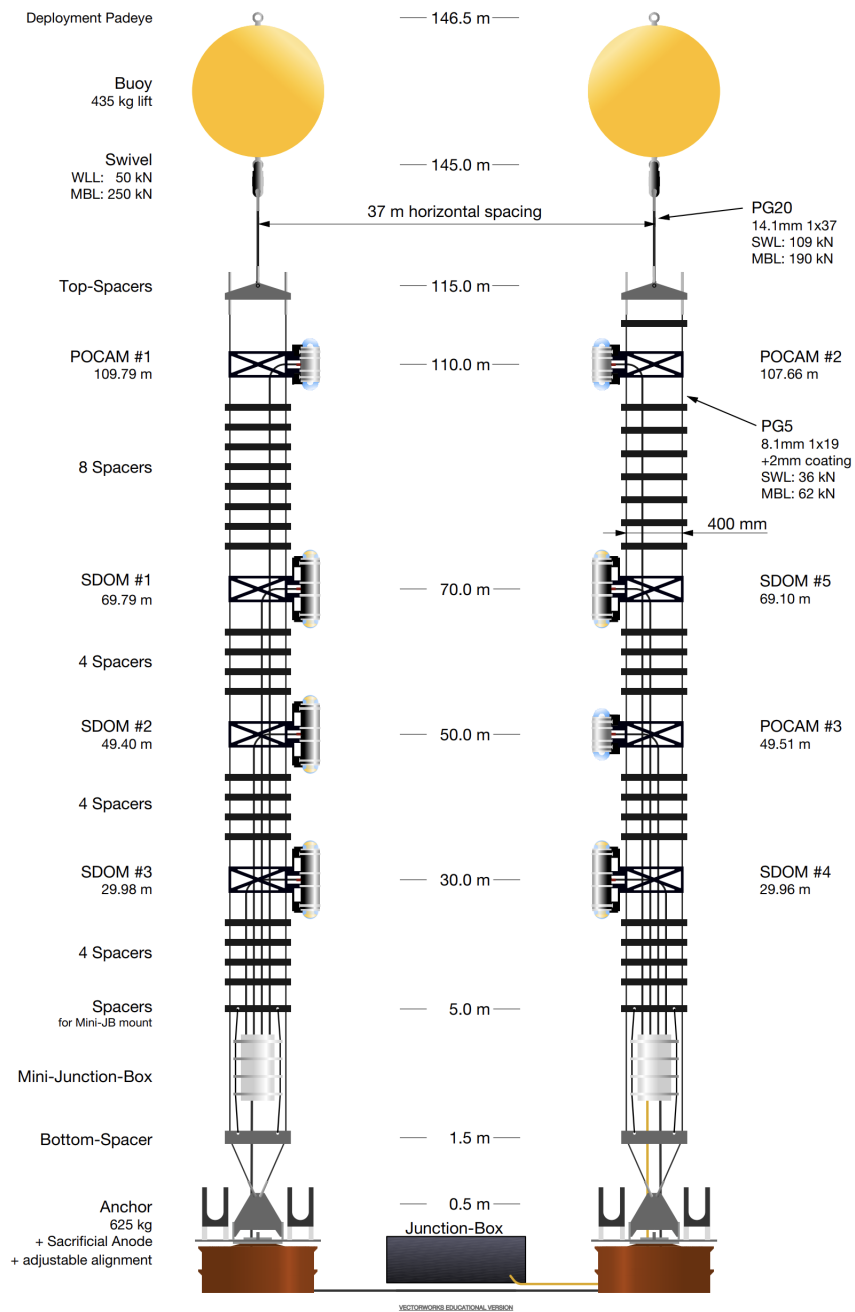


Figure 3.6: Schematic of the two mooring lines from the STRAW mission. Each optical module has got a couple of PMTs facing opposite directions.[34]

STRAW results on attenuation length, ^{40}K decay and bioluminescence rates after 4 years are the baseline on which the trigger mechanism analysis will be conducted.[36]

3.3.1 Attenuation Length

The primary analysis of the paper was concentrated on the optical attenuation length of the seawater. Light was emitted from the POCAMs with intensity I_0 . Travelling through water, absorption and scattering will reduce the initial intensity of the light. With the light detected by the sDOMs from the POCAMS, the fraction of events detected is used to estimate the attenuation length.

When considering the intensity measured at a distance, it's important to note that scattered light, although contributing to the overall measurement, follows a longer path than direct light, resulting in a delayed arrival. Utilizing timing information becomes crucial in effectively filtering out scattered light, minimizing its impact on the measurement of attenuation length. However, it's worth acknowledging that due to imperfect timing because of dead time on the DAQ by high bioluminescence exceeding the DAQ capabilities, and another 70ns dead time after a pulse is detected, some scattered light may still influence the measurements. Previous studies conducted by ANTARES[37] and Baikal-GVD[38] have observed that scattering in water is significantly weaker than absorption. Consequently, the absorption length is anticipated to be the primary factor contributing to the attenuation length.

In order to validate the methodology outlined earlier, Geant4 was employed for simulating the STRAW setup.[33] The simulation involved a simplified representation of the sDOMs as spheres to enhance computational efficiency, with multiple sDOMs placed in the simulation volume for increased statistical accuracy. The POCAMs were simulated as isotropic point sources, and the actual angular emission and detection profiles were incorporated through result reweighting.

The simulation focused on a single absorption length of 60m, and the results were adjusted based on the total light path of each simulated photon.

The Geant4 fit served as a comprehensive examination tool, utilizing both simulated and real data to cross-verify and scrutinize the results. Table 3.2 shows the

comparative results of the measured and simulated attenuation lengths.

Wavelength	Measured Attenuation Length	Simulated Attenuation Length
365nm	$10.4^{+0.4}_{-0.3}$ m	12.4 ± 2.6 m
400nm	$14.6^{+0.4}_{-0.6}$ m	16.1 ± 2.2 m
450nm	$27.7^{+1.9}_{-1.3}$ m	29.4 ± 3.5 m
585nm	$7.1^{+0.4}_{-0.3}$ m	9.3 ± 2.2 m

Table 3.2: Results of the measured attenuation length compared to the Geant4 cross-check for different wavelengths.[33]

Some large neutrino experiments have already measured their corresponding absorption and effective scattering lengths, such as IceCube, Baikal-GVD and Km3Net at wavelengths of 450nm. Refer to table 3.3 to see the attenuation lengths from these experiments. From the timing reconstruction limitations, the scattering length from STRAW cannot be measured, but it is assumed very low compared to the absorption length, so the latter is considered to be the attenuation length[33], but the estimation of the attenuation length is valid from the statistical approach in their measurements and the cross-check in Geant4.

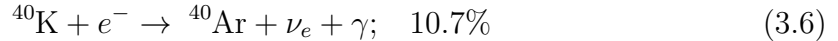
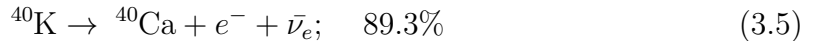
Site	Attenuation Length (L_{att}) [m]
Lake Baikal, 1km depth	16-20
Km3Net, ≥ 1.5 km depth	33-56
IceCube, 1.5-2.0km depth	≈ 16
IceCube, 2.2-2.5km depth	23-29
P-ONE, ≥ 2.5 km depth	26.4-29.6

Table 3.3: Attenuation lengths from different neutrino experiment locations: Baikal-GVD, km3Net, IceCube and STRAW respectively. From the timing reconstruction limitations, the scattering length from STRAW cannot be measured, but it is assumed very low compared to the absorption length, so the latter is considered to be the attenuation length.[33] Recovered from [27].

3.3.2 Potassium-40 Decay

STRAW measured the ambient light present in the deep ocean background. This is essential for developing a trigger mechanism in P-ONE. While the noise consists in stochastic spikes of bioluminescent events, there is a continuous noise floor due to radioactive isotopes decay, mainly potassium-40 (^{40}K) decays.[33]

^{40}K can decay into two main channels[39]:



The first one corresponds to β^- decay and produces electrons that emit Cherenkov photons. The second one corresponds to electron capture, where the photon released by the Argon nucleus can generate electrons through Compton scattering, hence producing Cherenkov photons. Cherenkov photons are then read by the optical modules as ambient background.

In the STRAW paper [33], the collaboration compared a GEANT-4 simulation with the read signal from STRAW.

The simulation was devised, featuring an sDOM positioned at the centre of a 25m radius sphere submerged in seawater. Owing to the back-to-back PMT configuration of the sDOMs, the majority of coincident ^{40}K photons arrive at large angles relative to the PMTs, resulting in reduced sDOM acceptance. The simulated seawater characteristics incorporate the attenuation length.

The simulation considers both decay channels, β^- decay and electron capture. Decay products, generated based on the total ^{40}K activity, are randomly distributed throughout the volume over a period equivalent to 3.0 minutes.

They found a consistent behaviour with the simulation to what was happening in the ocean depths as can be seen in figure 3.7. Having this simulation was imperative,

because it allows to calculate and predict the fraction of time a PMT was at an specific noise rate. The trigger development must consider the noise accidental triggers for the efficiency estimations at all times.

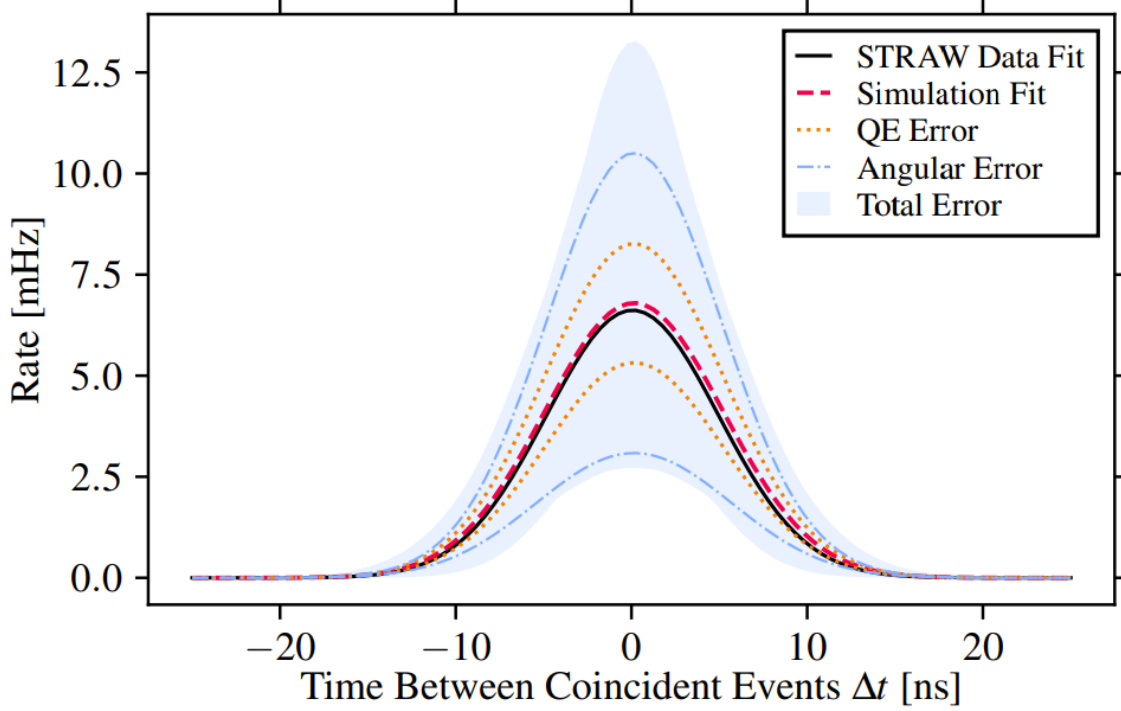


Figure 3.7: Gaussian fits to coincident detection rate distributions of STRAW data with the baseline subtracted (black) and simulation (red) plotted with the total systematic error band (blue). The dotted and dashed-dotted lines represent bands corresponding to the error contributions from quantum efficiency (QE), which is the ratio of how well can a PMT convert incoming photons into a detectable signal, (orange) and angular acceptance (blue).[33]

With the validation provided from the Geant4 cross-check, the results of the study for a 20ns window shown in figure 3.8 display a 100kHz minimum ^{40}K decay background rate per optical module, for two coincidences the rate is 1kHz, and for three coincidences it is 40Hz. Very low rates at higher-level coincidences are expected, compared to the atmospheric neutrino flux background [40].

3.3.3 Bioluminescence

Additionally to ^{40}K decays, there is bioluminescence in seawater. Bioluminescence is an emission of light by a living organism triggered by either a mechanical or physi-

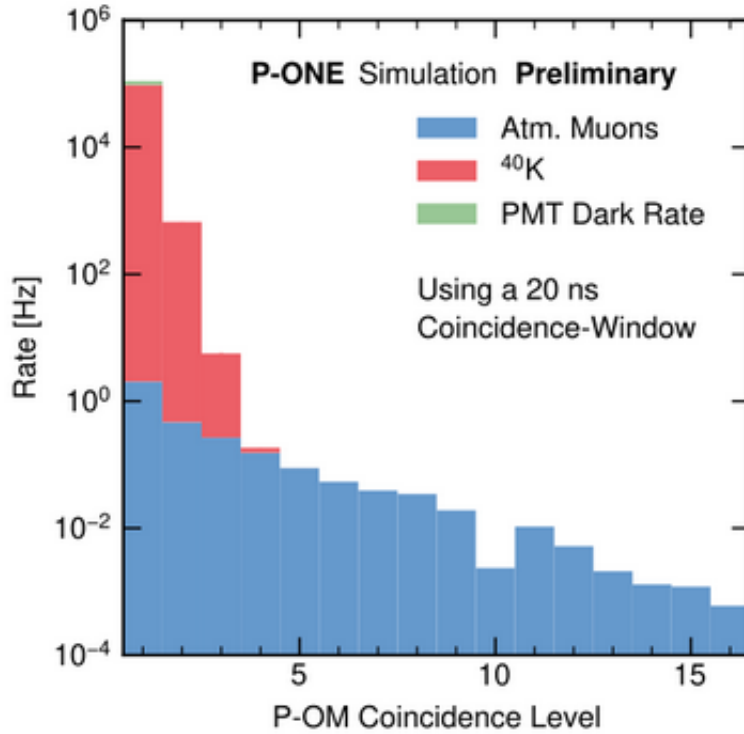


Figure 3.8: Distribution of the levels of PMT coincidences in an Optical Module and the total rate from ^{40}K . Additional distributions of PMT dark noise and Atm. Muons are included.[41]

ological stimulation. In a marine environment, it is a pervasive mechanism used by many species from bacteria to fish, for finding food, attracting mates and evading predators.[42] Moreover, it is believed that 75%[42] of all organisms larger than 1cm living between the surface and a depth of 4000m are capable of bioluminescence.[43]

A characterization of this phenomenon was imperative to quantify the impact on the detector trigger mechanism. An optimal trigger strategy will be a balance between the signal efficiency versus background rejection at high rates. Structures exposed to turbulent flows are known to trigger bioluminescence [44]. STRAW performed a 2 year monitoring of bioluminescence in order to address the problem.

The recorded rates primarily stem from three factors: photomultiplier dark noise, ^{40}K radioactive decays, and ambient bioluminescence. This combination is subject to variation based on different environmental circumstances.

Analysis of the data involves examining the range of rates for the lowest sDOM threshold, set at half the single photo-electron level. Rates are measured within a 30ms window. The study explores the distribution of rates over a two-year period and the temporal variations in these rates. To mitigate the impact of rates exceeding DAQ capabilities for a small fraction of time, the analysis focuses on percentiles rather than mean values, as they remain unaffected by such occurrences.

An illustrative example presents two minutes of data for the upper PMT of sDOM1 in Figure 3.9.

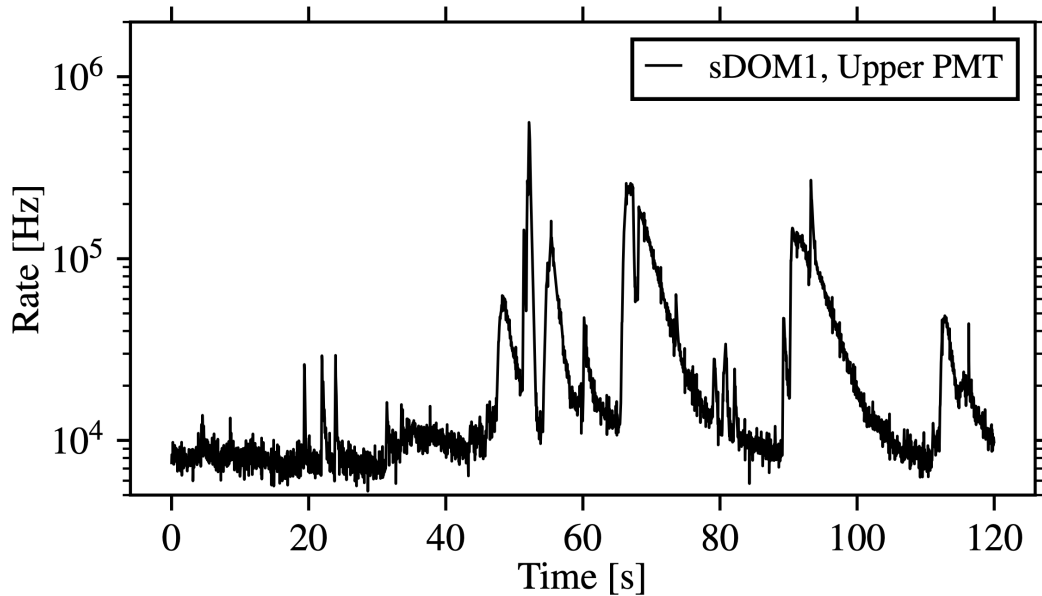


Figure 3.9: Rate of a single photomultiplier over two minutes, measured in 30ms intervals. There is a characteristic structure of a constant background rate with spikes caused by bioluminescence.[33]

The depiction of rate distribution spanning a two-year period is illustrated in Figure 3.10 (upper plot). The lower limit corresponds to the baseline level attributed to ^{40}K and dark noise, while the bioluminescence rates exhibit considerable variability, occasionally surpassing the maximum detection rate of 10MHz. This information serves as a fundamental input for shaping the future P-ONE DAQ system. Notice the 50% percentile is at the 50kHz rate mark, indicating the median fraction of time

the detector will be under that rate. Additionally, the lower plot in Figure 3.10 presents the computed fraction of time above a given rate, providing insight into estimating the bioluminescence-induced dead-time of such a DAQ system.

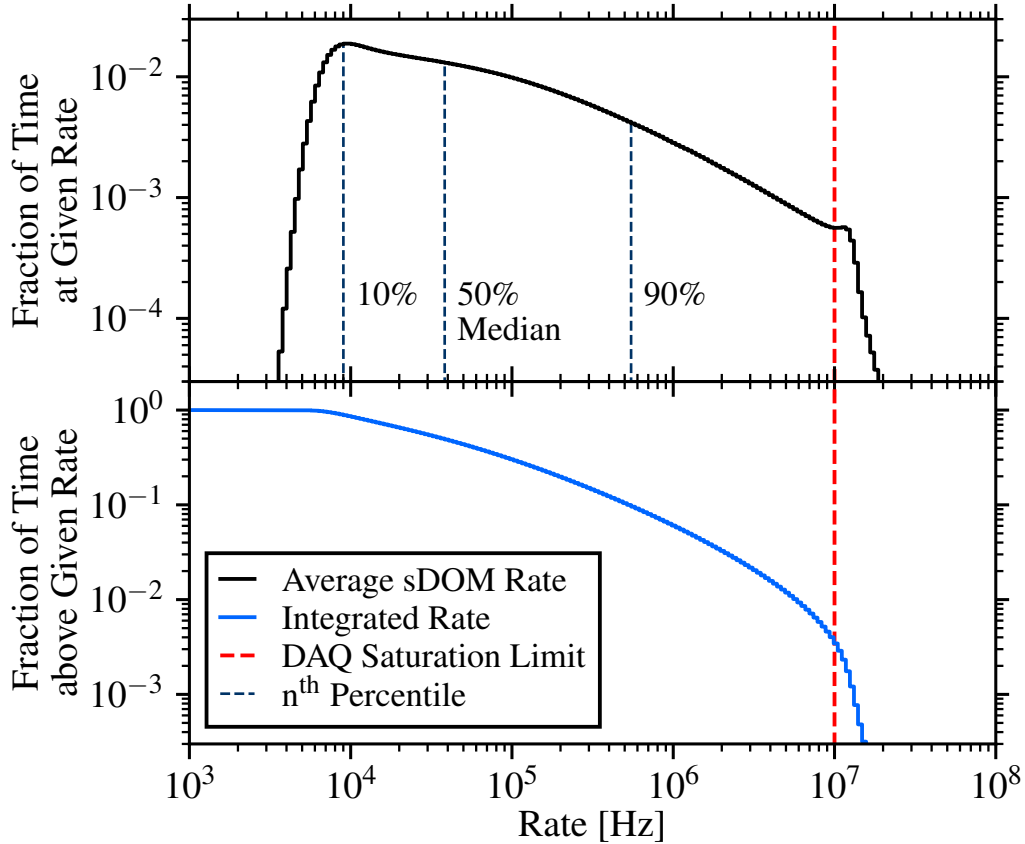


Figure 3.10: Distribution of a single PMT background rates measured over two years of STRAW. The bottom plot shows the integral fraction of time from a given rate to infinity, showing from which fraction of time a certain rate was exceeded.[33]

This results allowed us to calculate the accidental trigger rate produced by background noise from which a detector trigger mechanism can be developed.

3.4 Detection of Muon Tracks and Cascades

Depending on the interaction type described in chapter 2 and their subsequent secondary particles, different event topologies are seen inside a detector. Generally, they can be classified as so-called cascades, tracks, and double bangs. Exemplary events

of those topologies recorded in IceCube are shown in figure 3.11.

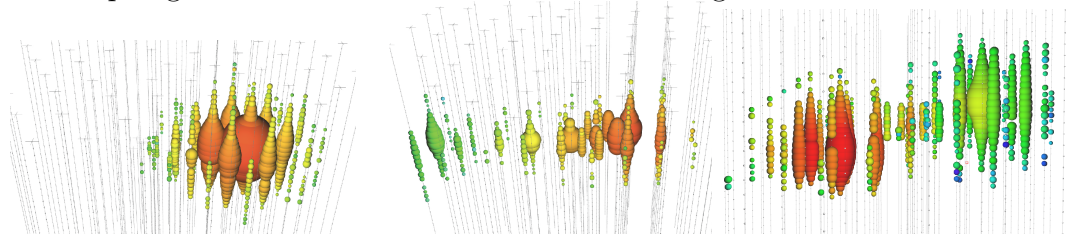


Figure 3.11: Illustration of a cascade (left), a track (middle), and a double bang (right) recorded in the IceCube Observatory. The spheres represent the optical modules with their size correlating to the detected amount of photons and their colour to the photon arrival time. Figures from [45].

In charged-current neutrino interactions, encompassing neutrinos of any flavor interacting with a nucleon to produce a lepton and a hadronic shower, specific manifestations arise depending on the neutrino flavor involved.

For ν_μ CC processes, the outcome is characterized by the presence of a discernible muon track alongside hadronic cascade. In the case of ν_e interactions, the result manifests as electromagnetic cascades. Meanwhile, the ν_τ CC process stands out with its distinctive double-bang signature. This unique signature can take the form of two cascades or a singular cascade, succeeded by a muon track, culminating into another cascade. The specific nature of the τ decay mode dictates the observed pattern.

3.4.1 Muon Tracks

In the muon track case, high energy neutrinos are inferred from the Cherenkov cone accompanying muons. It is crucial to distinguish the signatures of upward going neutrinos, because the background of this signature are very low because the Earth works as a natural filter from particles coming from that direction. For this reason, the effective volume of the detector is larger than the actual dimensions of the detector given the long distances muons can travel depending on energy (1km at 300GeV to 24km at 1Pev)[46]. As the muon travels it loses energy via ionization, bremsstahlung and photonuclear reactions.[46]

Ionization occurs when a muon, interacts with atoms in a material, displacing electrons from their orbits and creating ion pairs (positively charged ions and free electrons). Bremsstrahlung, which means "braking radiation" in German, occurs when a charged particle, like a muon, is deflected by the electric field of a nucleus and emits a photon. Muons can lose energy through interactions with photons that subsequently undergo photonuclear reactions. These effects can be parameterized by[47]:

$$-\frac{dE_\mu}{dx} = a + b \cdot E_\mu$$

For water, the ionization loss is given by $a = 2\text{MeV/cm}$, the energy loss from bremsstrahlung and photonuclear reactions is described by $b = (1.8+1.6) \cdot 10^{-6}\text{cm}^{-1} = 3.4 \cdot 10^{-6}\text{cm}^{-1}$ and rises linearly with energy.[22] See figure 3.12 where it shows dE_μ/dx as a function of E_μ for different materials.

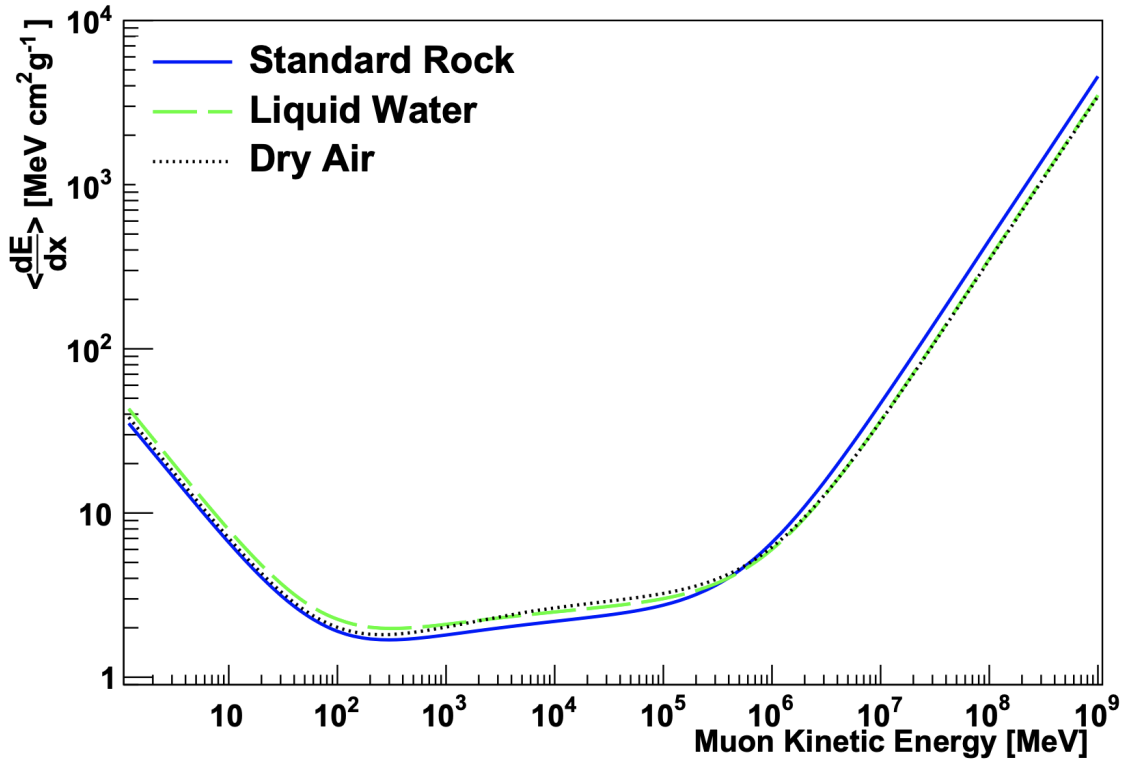


Figure 3.12: Energy loss of muons for different materials. The plotted data is taken from the Particle Data Group tables in [48].

Underwater/ice telescopes are optimized for the detection of muons over 1TeV, because at higher energies the muons interact more with matter generating more light, as well as having a longer track making them easier to detect.[7, 49]

3.4.2 Cascades

Charged current interactions of electron neutrinos lead to electro-magnetic cascades and most tau neutrinos lead to hadronic cascades. Cascade events could be considered as point like sources of light depending on the layout of the detector. The effective volume of a detector experiment for cascade events is almost the same geometry of the detector volume, because the particle interaction only can occur inside the volume for it to be detectable. See figure 3.11.

The amount of light emitted depends on the energy of the original neutrino. There are no measurements of dE_μ/dx for cascades because they do not leave a track in the detector. However, the energy of the neutrino can be better determined because the whole interaction occurs inside the detector volume. [22]

3.5 Neutrino Telescopes

3.5.1 IceCube

IceCube stands as the largest and most successful underwater/ice neutrino experiments, marking the world's first 1km³ neutrino telescope. Fully operational since 2010, IceCube's construction commenced in the early 2000s following the triumph of the AMANDA pathfinder mission [50]. The detector comprises 86 strings, each hosting 60 Optical Modules, extending 1km in longitude beneath the Antarctic ice, with the additional presence of DeepCore, a denser array strategically located at the center for optimized low-energy event detection [51]. Notably, IceCube achieved a milestone in 2013 by detecting 28 high-energy extraterrestrial neutrinos, indicating a non-atmospheric origin and sparking discussions on potential extraterrestrial accelerator sources [1]. In 2017, IceCube identified the blazar TXS0506 + 056 as a likely

source of extragalactic neutrinos, correlating a gamma-ray flare with the neutrino detection event [2]. Additionally, in 2022, they detected neutrino emission above 1 TeV from the active galaxy NGC 1068, confirming a second source of extragalactic neutrinos.[3] These groundbreaking results have paved the way for an extensive search for neutrino sources and characterization. IceCube’s future endeavors include the IceCube-Gen2 upgrade, aiming to enlarge the detector to 8 km³ with 1000 new Optical Modules, thereby enhancing angular resolution and sensitivity to neutrino oscillations [52, 53].

3.5.2 Km3Net

KM3NeT[54] is another neutrino telescope experiment being installed in the deep Mediterranean Sea. It is the product of a combination of different experiment infrastructures like NEMO[55], NESTOR[56] and ANTARES[37]. They are located in two different spots in the sea, resulting in a network of detectors.

Besides the obvious difference from IceCube, that this experiment is underwater instead of ice, is that KM3NeT opted for a multi-PMT approach for its Optical Modules. Once finished, KM3NeT will be composed by two detector arrays, ARCA[57] (Astroparticle Research with Cosmics in the Abyss) and ORCA (Oscillation Research with Cosmics in the Abyss) at its two locations respectively. As of September 2022, 21 strings were already taking data and transmitting it to shore.[58] ARCA site will be divided in two clusters, each 500m in radius. And it will focus on high energy detection of neutrinos, whereas ORCA, located on the other site, will be only a single cluster of 100m of diameter; its goal is to study fundamental properties of neutrinos.[59]

3.5.3 Baikal-GVD

Situated in Lake Baikal, Russia, at a depth of approximately 1km, the Gigaton Volume Detector (Baikal-GVD) is a neutrino telescope characterized by a clustered structure. Each cluster comprises 8 strings, and each string accommodates 36 optical

modules. The strings are positioned 60m apart, with clusters separated by 300m.[60, 61] As of April 2022, ten clusters have been deployed and are operational, with plans for a total of 16–18 clusters by 2025–2026, resulting in a detector volume exceeding 1km^3 [60]. However, the project faced a setback with the termination of Western support in early 2022, leaving uncertainties about the extent to which Baikal-GVD will contribute to scientific advancements in the near future.

Chapter 4

Simulation

The first P-ONE string is slated to be deployed in the Summer of 2025. Therefore, the analysis in this thesis can only be done through simulation and with the data recovered from the STRAW experiment for the estimation of the bioluminescence.

The way to estimate the trigger efficiency of the 10-string P-ONE detector before its deployment is by simulating particle events underwater under different conditions and measure the trigger efficiency of those events when interacting with the detector. One study will focus on the geometry optimization of the detector, by generating a muon neutrino flux, the next one will address the detector response for 10 TeV muons (track) events and the last one will focus on the trigger efficiency for all neutrino flavours at different energies.

4.1 IceTray

The IceCube experiment developed a framework used for particle simulation and analysis called IceTray. Since P-ONE is also a high energy neutrino experiment and both have a similar detector layout; with PMTs and Optical Modules, the simulations conducted in this analysis used IceTray. This framework can host and run all the libraries and algorithms necessary to simulate events similar to those we find on P-ONE.[62]

The framework is written with the intention of being modular. A modular de-

sign means breaking down a system into smaller, independent, and interchangeable modules. Each module focuses on a specific aspect or functionality of the simulation, i.e. particle propagation module. Modules can be added, removed or edited in the working space or "tray" by the users. Additionally, the core framework is written in C++ for speed with Python used for configuration. Users have the option to write their modules using either C++ or Python.

The simulation process includes a particle generator module like *MuonGun* or *LeptonInjector*, a particle propagator; *PROPOSAL*, a photon propagator; *CLSim*, an Optical Module Response mechanism, and finally a Trigger mechanism. Moreover, *LeptonWeighter* is a module used for weighting the sample of generated neutrinos to a particular neutrino flux, if needed. In the following sections a description of each module will be covered. Figure 4.1 shows an example of the structure of a complete simulation. The resulting data of the Optical Module Response were then used to develop the Trigger Mechanism.

4.2 Muon Neutrino Flux

The first simulation was of a muon neutrino flux. The purpose of this simulation is to determine the best detector size for detecting events of interest. For the generation of muon neutrinos, *LeptonInjector* was used. *LeptonInjector* is capable of simulating neutrino events of all flavours over a wide range of energies from 10 GeV to 100 PeV, undergoing neutrino-nucleon interactions in the Deep Inelastic Scattering (DIS) regime and antineutrino-electron scattering producing W in a Glashow Resonance (GR) interaction, ($\bar{\nu}_e + e^- \rightarrow W^-$). The initial event energy sampled accords to a single power-law spectrum, and final state kinematics are sampled from spline interpolations of the differential cross sections for the relevant interaction. [63]

The neutrino energies were sampled from 10TeV to 10PeV following a E^{-2} power law. This means that the probability of sampling a particle with energy E is proportional to a E^{-2} distribution. Since P-ONE is intended to be optimized for high

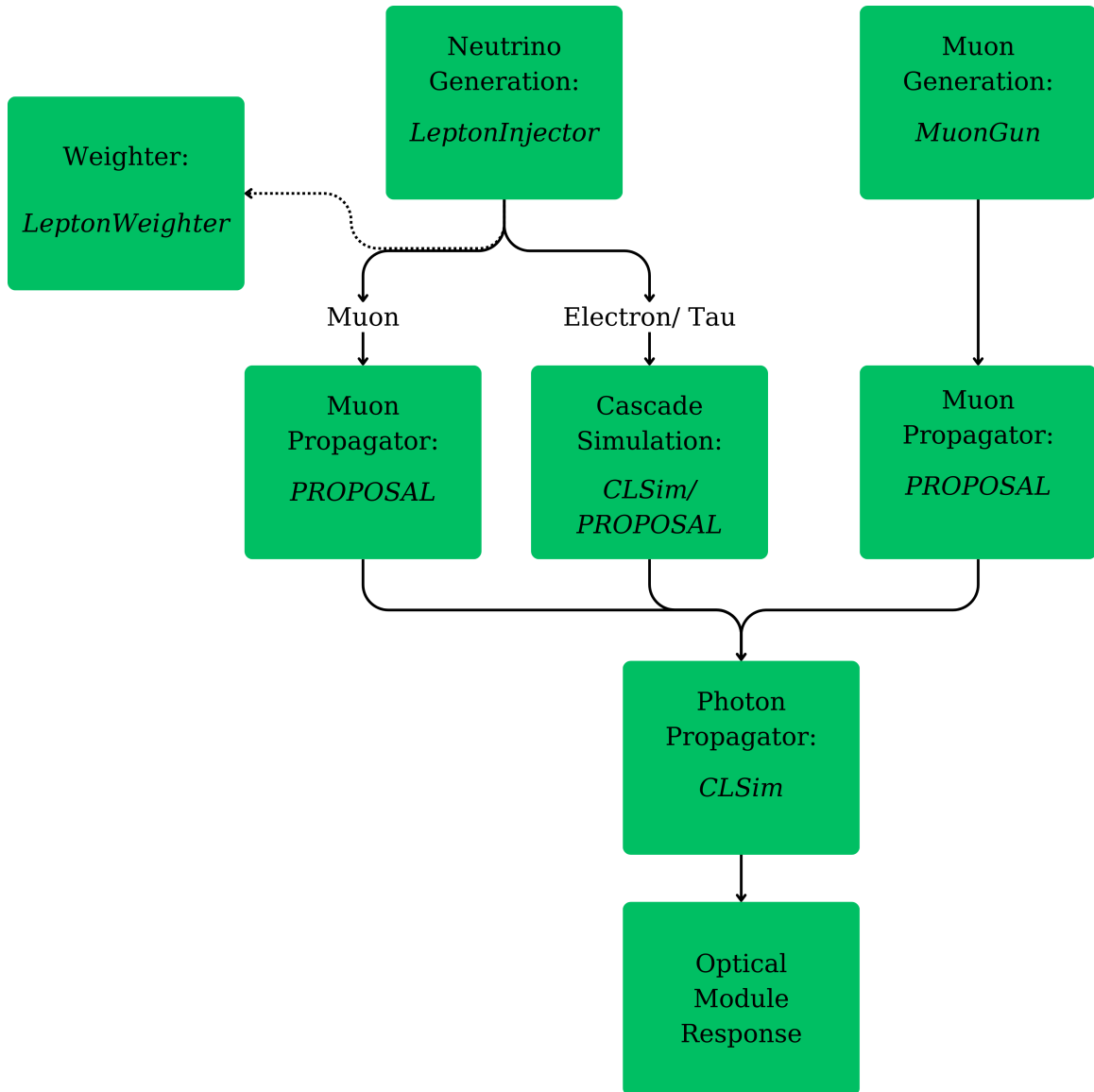


Figure 4.1: Illustrative process of a simulation. Each box represents a module in the "tray", and the output of each module becomes the input of the next one if they are connected. First, generate neutrino with *LeptonInjector*, if the selected neutrino flavour is muon, then the muon track is propagated using *PROPOSAL*. The generated sample can also be weighted to a neutrino flux with *LeptonWeighter*. If the selected neutrino flavour was electron or tau, then a cascade simulation occurs, but since a tau can decay into a muon, *PROPOSAL* is also used for the muon propagation. After the particle propagation, there comes the photon propagation with *CLSim*, and the last module is the *Optical Module Response*. The process is similar for the generation of muons with *MuonGun*. Details of each module is covered in sections 4.2, 4.3 and 4.6.

energy events, the starting sampling energy is at 10TeV. In the process of generating muon neutrinos, the primary neutrino's direction is initially chosen. Subsequently, a random point is selected from a disk with a radius equal to the detector radius, centered at the origin and perpendicular to the previously determined direction. This chosen point becomes the point of closest approach (PCA) for the projected path of the injected neutrino. The distance from this sampled PCA to the origin is referred to as the impact parameter.

Following the determination of the impact parameter, a range of potential positions along the neutrino's path is established, allowing for the sampling of the interaction position. This range includes two "endcaps", defined by lengths on both sides of the disk containing the PCA. The purpose of these endcaps is to ensure that events are sampled across the entire volume of the detector. This comprehensive approach enables the sampling of interaction positions in a manner that considers the entire detector volume.[63]

During the muon neutrino interaction, a fraction of its energy will go to a resulting muon and the rest turns into a hadronic shower. The resulting muon is the particle easiest to detect, since it leaves a muon track within the detector volume. PROPOSAL (Propagator with Optimal Precision and Optimized Speed for All Leptons)[64], is a public tool used for propagating leptons. It includes cross sections for ionization, bremsstrahlung, photonuclear interactions, electron pair production, muon and tau decay, etc.[64] PROPOSAL takes care of propagating the muon until it gets outside of the detector's detection range.

The muon track emits photons along its path that are also propagated considering the properties of the medium, such as absorption/scattering lengths too. The CLSim [65] module handled this part of the process.

CLSim's first step in simulating the light yield from a given particle at an Optical Module is to convert the particle into a series of light-emitting "steps". Each step is assumed to move at the speed of light, determining the Cherenkov angle and

calculating the number of photons that should be emitted over a given length. The set of steps generated are run in "kernels" in parallel using GPU, propagating the photons through the medium and checking for collisions with Optical Modules. All photons that collided with any PMT in the Optical Module are saved with their full information. The output of the GPU simulation step is thus a list of photons at the Optical Module surface.[65]

The process was repeated six times with different geometries of the detector. Each simulation ran with inter-string separations of 50m, 60m, 70m, 80m, 90m, and 100m.

After the events are generated and propagated I weighted them using LeptonWeighter. LeptonWeighter weights each event so that it matches a physical neutrino flux and interaction cross section. [63] The chosen fluxes were the sum of the Atmospheric and Astrophysical neutrino flux, obtained from nflux, an IceCube library used for calculating the neutrino flux.[66] The cross section used were the DIS of a muon neutrino for charged current interactions. These were obtained from photospline which is another IceCube library used for calculating neutrino cross sections.[67]

To reweight a sample of events, LeptonWeighter first calculates the probability density that the LeptonInjector generator could have produced an event for each event with equation 4.1[63, 68], where N_{gen} is the total number of generated events, Ω_{gen} is the solid angles over which events were generated, A_{gen} is the integrated area of the sampling surface, $\rho_{gen}(l)$ is the local mass density of targets, X_{gen}^{col} is the total column depth of targets in the sampling region, $\partial_{xy}\sigma$ and σ_{tot} are the differential and total cross-sections evaluated for the event, respectively and $\Phi(E)$ is the power-law flux spectrum of the generator.

$$P_{MC} = N_{gen} \frac{1}{\Omega_{gen} A_{gen}} \times \frac{\rho_{gen}(l)}{X_{gen}^{col}} \times \frac{1}{\sigma_{tot}} \frac{\partial^2 \sigma}{\sigma_x \sigma_y} \times \frac{\Phi(E)}{\int_{E_{min}}^{E_{max}} \Phi(E) dE} \quad (4.1)$$

With the probability density we can now calculate the generator weight by inverting

equation 4.1:

$$w_{gen} = \frac{1}{P_{mc}}$$

Finally the weight of each event for a selected flux is approximately given by equation 4.2

$$w_{event} = \rho_{physical} \times \Phi_{flux} \times w_{gen} \quad (4.2)$$

Where $\rho_{physical}$ is the probability of the particle interacting with a nucleus on its path as long as the interaction occurs within the detector volume and up to 80m outside of it, Φ_{flux} is the desired neutrino flux and the w_{gen} is the previously calculated weight of the generation. After all proper calculations it gives you the weight of each event with units of s^{-1} .

This weight corresponds to the number of events that share the same characteristics in flux that can be generated in a second, so I multiplied the weight by 1 year in seconds to count the number of events that share the same features in a year.

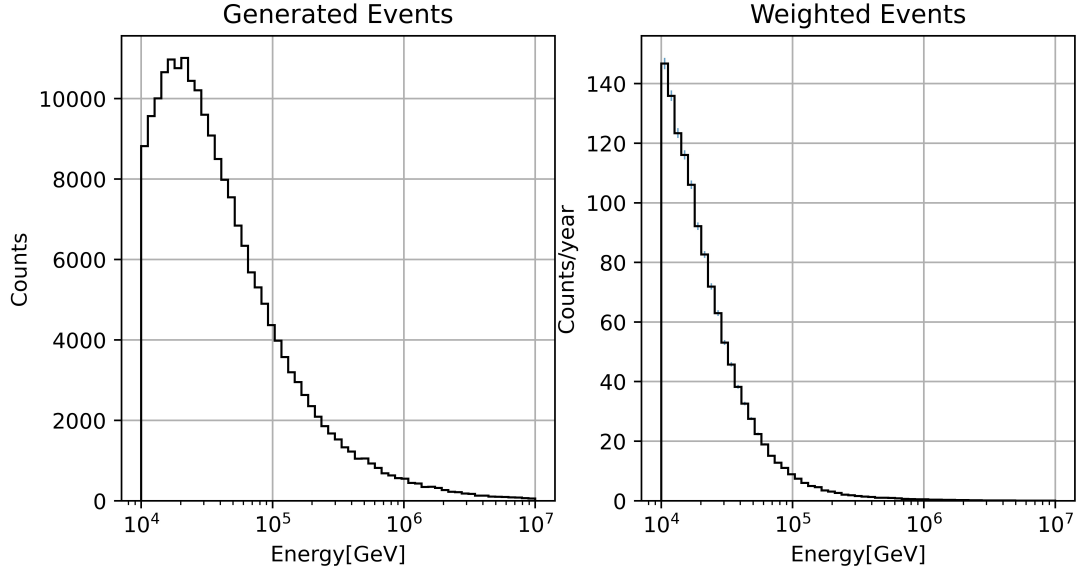


Figure 4.2: Energy distribution of sample events. On the left is the default sample of events generated. On the right is the weighted energy distribution of the original sample measured in counts per year.

As we can see in figure 4.2, the selected flux shows a larger number of lower energy events, and rapidly decreases the number of events at higher energies.

With the weight of the event and the photon hit list we can proceed to the Optical Module Launcher module. This module is unchanged for all simulations so it will be listed later on this chapter in section 4.6.

4.3 Monoenergetic Muons

The next simulation consists in monoenergetic muons injected isotropically into a 10-string detector, with inter-string separation of 80m, just like in figure 3.3 in earlier chapters, which was the selected geometry for the detector from the results that will be discussed in section 5.4. The aim of this simulation is to optimize the efficiency of the trigger algorithm. Since muons leave tracks inside the detector volume, the developed trigger algorithm works for detecting that signature. MuonGun was used the selected generator of muons to address this analysis. MuonGun is a toolkit that can efficiently generate a muon flux at desired energies. The radius of injection was 80m outside the detector volume to avoid stochastic losses of the muon energy before going inside the detector.

Once the muon is generated, it is propagated using PROPOSAL and subsequently into CLSim just like the previous simulation. This time around, there is no need to perform any weighting because we are not interested in any particular flux. After CLSim, we get the list of photons at the Optical Module surface.

4.4 Muon Neutrino Full Energy Spectrum

After knowing the efficiency of the trigger shown in section 5.5.3, the third simulation happens. Therefore the purpose of this simulation is to estimate the overall efficiency of the trigger for muon neutrinos at different energies.

Similarly to the muon neutrino flux simulation, LeptonInjector was used to generate muon neutrino interactions. This time however, the energy spectrum ranged from 100GeV to 10PeV, but the energy distribution was flat. As mentioned earlier, the

goal is to obtain a value of efficiency at each energy level, that is why multiple events at each energy bin was generated. Each muon was then propagated with PROPOSAL and CLSim, yielding the list of photons at the Optical Module Surface.

4.5 Cascade Simulation Full Energy Spectrum

Finally, a cascade simulation is needed for the production of an electron neutrino or a tau neutrino. Both either decay shortly after production or lose energy shortly after production, so the signature looks like a sphere of light with a point-like source. The size of the sphere depends on the energy of the particle because it emits more light.

For the case of cascade simulations, a range from 100GeV to 10PeV neutrinos was generated with LeptonInjector on the same geometry as the previous simulations. In both tau and electron neutrinos, their charged current interaction cross sections were used. The energy distribution was flat, because the intention of this simulation was to estimate the efficiency of the triggers proposed at different energies.

For the case of tau neutrinos, PROPOSAL was also used for their propagation, because tau sometimes decay in muons leaving a track in the detector. On the other hand, electron neutrinos cascades occur in such a rapid manner, that there is no need for a propagation of the particle. CLSim then, handles both the propagation of the photons of the electron cascades and tau cascades. Finally, we obtain the list of photons at the Optical Module Surface.

4.6 Optical Module Response

The last aspect that needs to be simulated for all three simulation cases, is the PMT response of each Digital Optical Module (DOM). This means producing the pulses from the propagated photons that hit a particular PMT. The directionality of the photon and the energy were the parameters used to determine if the photon was absorbed by the PMT, and from that build an electric signal that represents a hit on

a PMT.

The resulting data of this simulation is a mapping of all the registered pulses per DOM, meaning that it recovers all the hits per PMT, per DOM across the whole detector module; it also includes the time of the hit and the charge. The Optical Module Response module depends highly on the geometry of the detector, so this section also looks into the geometry file to create the hits. The implications of a varying geometry will be discussed later.

An example of a simulation output is shown in the Appendix A.

Chapter 5

Trigger Algorithm

Despite the ultimate configuration of the P-ONE detector as a 7-cluster system, each cluster comprising 10 strings, our trigger design is currently tailored for a 10-string cluster, because the bandwidth limits available as of the writing of this thesis only allow for a 10-string detector, which is the first stage of the experiment. Nevertheless the chosen trigger architecture is also scalable when additional number of strings are deployed as long as the bandwidth available for read out scales too.

The primary challenge that requires careful consideration is regarding the substantial noise signal originating from ^{40}K and bioluminescence in the underwater environment, in conjunction with the bandwidth constraints imposed by the chosen hardware for detector construction. As previously discussed, the estimated maximum bandwidth capacity of the P-ONE electronics stands at 8000Hz for detector readout. Consequently, any trigger algorithm chosen must adhere to this maximum bandwidth threshold.

5.1 Noise Rate Trigger

To tackle this issue, I calculated the accidental trigger rates expected, based on the light noise rate present in the region. First, let us remember that the whole detector volume consists of 200 DOMs, so if we divide the maximum available rate over the total number of DOMs, we get the maximum single DOM rate that we can work with.

In this particular case, it is only 40Hz.

From the bioluminescence information recovered from STRAW, we have a distribution of the fraction of time at which the PMTs in a module were at a certain average rate of bioluminescence as seen in figure 3.10. Knowing this, and knowing that there is an average 10kHz rate on all PMTs constantly, from the prevalent ^{40}K decays, we can obtain the accidental trigger rate per individual DOM as a function of the number of PMT coincidences in a DOM. There are a couple of assumptions that have to be made in order to calculate this:

- There is no correlation between DOMs when a bioluminescent event is happening. This means that there is no correlation in bioluminescence noise rates between different DOMs. At the same time, the bioluminescence is uncorrelated on the timescale of PMT coincidences. The random noise rate per PMT in a DOM is correlated but the individual noise hits are not.
- Only half of the DOM will be affected by the bioluminescence for the duration of the event.

The first assumption finds support in the data from STRAW, which demonstrated that when one optical module experienced a sustained high-rate event, the remaining optical modules continued to operate at their standard signal rates. Figure 3.9 shows how a bioluminescence event can take multiple seconds to go through whereas the PMT coincidence rate will be only 10ns, hence the assumption is there is no correlation from bioluminescence at short timescales.

The second assumption, comes from our current knowledge that many living bioluminescent organisms emit light when disturbed by turbulence that occurs downstream of an obstacle, such as a P-ONE string. Given that half of the PMTs will be oriented to face upstream, we are thus assuming that only half the DOM will see the bioluminescence. It's important to note that the whole DOM will still detect the 10 kHz signal arising from ^{40}K decays.

The most intuitive, and easy to implement method to reduce a large rate of noise hits, is by demanding a certain number of PMT coincidences in a DOM within a certain period of time. Given the electronics we currently possess plus size of the DOM and the innate PMT's time resolution, a 10ns window is selected to count for all the PMT hits in a DOM. That is the time required for the light emitted by a passing muon to hit the full DOM in one trigger window.

Function 5.1 shows how to estimate the accidental noise rates, considering all the information above. If we are looking for multiple PMT coincidences, then there is a chance that one or more PMTs are on the side not facing the bioluminescence only the ^{40}K rate, and once again there are 8 possible PMTs to pick from on that half.

The single DOM average rate estimation, (sdr) is a sum of probabilities of all the possible PMT combinations depending on the number of coincidences required, n is the number of PMT coincidences and m is the number of PMT hits on the ^{40}K side of the detector. The argument of the sum starts with r , which is the bioluminescence rate read by a particular PMT, the K_{40} term represents the rate read by a PMT that is facing the non-bioluminescent side; it is a constant at 10kHz. Then we are considering all the combinatorics of PMTs and how they are split between the noisy and quiet sides of the DOM. The combinatorics function $nCm(8, n-m)$ is defined as:

$$nCm(8, n - m) = \frac{8!}{(n - m)!(8 - n - m)!}$$

. As mentioned earlier, a 10ns time window (t_w) is selected, so the coinciding rates should fall inside that time window. The t_f represents the fraction of the time we are at an specific r , according to STRAW results.[33] (See figure 3.10.)

$$sdr(n) = \sum_{m=0}^n r^{n-m} nCm(8, n - m) K_{40}^m nCm(8, m) t_w^{n-1} t_f \quad (5.1)$$

To explain this further, let us see the example of having 3 PMT hits while looking for a 3 PMT coincidence trigger.

$$sdr(3) = \sum_{m=0}^3 r^{3-m} nCm(8, 3-m) K_{40}^m nCm(8, m) t_w^2 t_f \quad (5.2)$$

As seen in equation 5.2, $n = 3$ so sdr is the sum of all the possible combinations in which the PMT hits can be found within the DOM. When $m = 0$, all the PMT hits happened on the half that had bioluminescence, whereas when $m = 3$, is the contribution from the case where all PMT hits might have occurred on the ^{40}K side. The same calculation was repeated starting from 2 PMTs in coincidence up to 5 PMTs as it is shown in Figure 5.1.

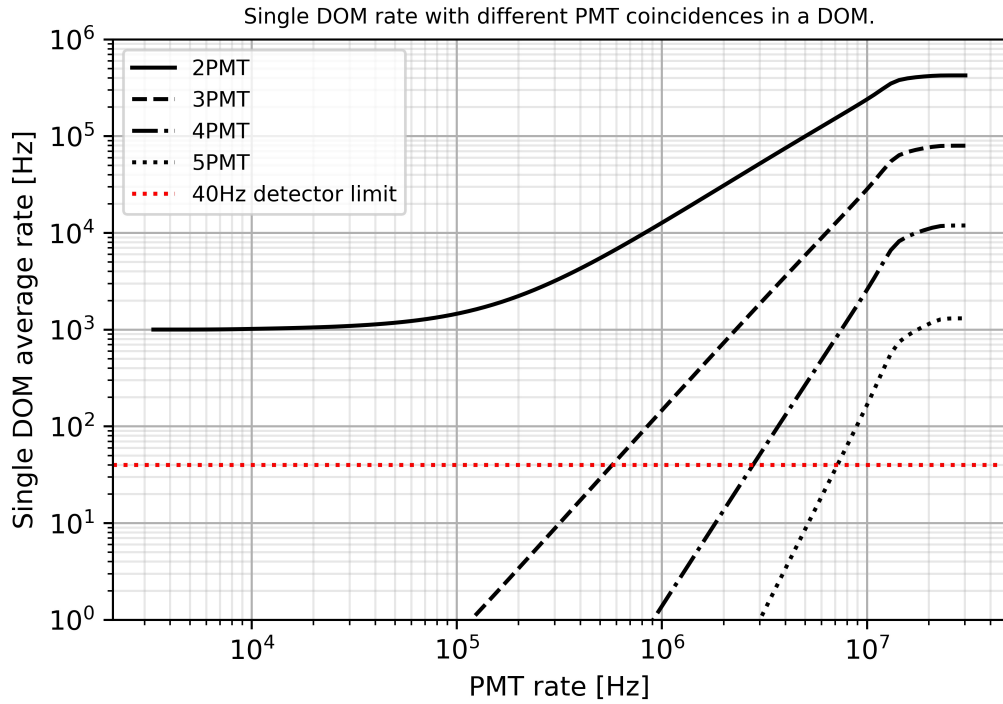


Figure 5.1: Average single DOM rate vs. PMT rate for different PMT coincidences in a DOM. The average single DOM is the maximum rate cut off for each single PMT with bioluminescence. The red dotted line marks the 40Hz limit available per DOM to trigger the detector.

Figure 5.1 shows that a trigger algorithm consisting on finding 2 PMT coincidences within a DOM is not enough to reduce the effects from the bioluminescence and K40 decays. So the most natural step forward is to think of 3 PMT coincidences or higher. However, the more coincidences required, the higher the effect on the efficiency of the detector. For the particular case of 3 PMT coincidences, the plot shows that we can

trigger on them, as long as the PMT rate is under 607kHz, per PMT. For 4 PMTs the rate should be under 2.95MHz, and so on.

The subsequent phase of the study involves estimating trigger efficiency through simulation. The overall efficiency will be scaled to a *dead time* factor that depends on the fraction time the detector is over the readout limit so that the average in a single DOM rate is 40Hz. This process aims to identify the optimal algorithm that adheres to the bandwidth constraints while maximizing the overall trigger efficiency.

5.2 DOM Trigger

As seen in Chapter 4, the last part of the simulation process produces a PMT pulse map that describes all the PMTs hit in a DOM, including the time stamp and PMT ID, for all DOMs in the detector. Although the simulation is controlled to only generate one particle per event, its full propagation may result in secondary particles that also decay and emit light. At the same time, due to the scattering properties of water, some other photons may change trajectories arriving later to the DOM, than if they would only travel in a straight line.

In order to avoid later incoming pulses, a time sorting discrimination algorithm was developed. Meaning that if a PMT hit was registered outside the 10ns window it is not considered as a valid hit for the PMT coincidences. The implementation of 10ns coincidence algorithm was the following:

- Sort all the PMT pulses by time of hit.
- Select the first hit to open the 10ns window.
- Add PMT hits inside the window to create the first set of coincidences. Each PMT can only be in the same set once.
- Look at the second PMT hit and open another 10ns window. Repeat until having a set of coincidences for all PMT hits.

- Compare the list of sets to the first one.
- If another set has got a larger number of coincidences, *and* it shares almost all of the same PMT hits as the first one, then the latter set is selected as coincidence.

Our preference is for the most PMTs in coincidence set, provided that it shares PMT hits in common with the first set registered. We accord higher priority to the first set that arrived due to the optical characteristics of water. Any scenario in which the earliest set is not chosen occurs only if the subsequent largest set includes some of the late PMT hits from the first set.

Label of set	Set	Selected	Reasoning
A	[1,2,3]	A	It arrived first.
B	[2,3,4]	A	Same number of coincidences.
C	[3,4,5,6]	C	Larger number of coincidences.
D	[7,8,9,10]	C	It keeps some of the PMT hits earlier in time.

Table 5.1: Example of a list of 10ns window sets sorted by time for a DOM. The number in each set represents the PMT Id, so set A is a 3 PMT coincidence of PMTs labeled 1, 2 and 3. Each PMT can only appear once per set. The *selected* column is the current set chosen as the coincidence. It starts by default with the first one to arrive and progressively iterates over the whole list of sets deciding what is the most optimal coincidence window for the event. After comparing all sets, set C is kept because of largest number of hits and also having an earlier time of capture than set D. That yields a 4 PMT coincidence for that DOM.

Table 5.1 is an example of a list of sets of an event sorted by time in a DOM after the 10ns windows discriminator. The numbers in the *Set* column represent the Id of the PMT hit. The first set is initially selected by default since it is the first to arrive. In this case, it is A representing 3 PMT hits, with IDs 1, 2 and 3. When compared to B (2,3,4), set A still is selected for having the same number of hits. Continuing the iteration to set C (3,4,5,6), it is selected over A because there is a larger number of PMT hits than A, so it is preferred. Lastly, there is another set with 4 PMT hits, but set D (7,8,9,10) arrives later than set C, so earliest is selected. The reason behind this is that PMT hits that arrived outside the 10ns window are considered either photons

from secondary particles or scattered photons. After the discriminator algorithm, a 4 PMT coincidence in a DOM (set C), was obtained in this example.

This algorithm is applied to all DOMs per event. The output of this simulation is the DOM trigger coincidence map, which is a list of all the DOMs that had PMT hit coincidences during the 10ns window, per event. This will allow us to continue the efficiency analysis. Although, there are some additional steps to be addressed first, such as the definition of a reconstructable event and the optimization of the detector geometry.

5.3 Selection of Reconstructable Events

The primary objective of a particle detector extends beyond mere particle detection; it centers on the capacity to extract meaningful information from the detector. In essence, this entails the ability to engage in physics. The actual analysis of the detected particles occurs subsequent to a reconstruction process that derives the particle's properties from the light deposited on the PMTs.

Reconstruction algorithms are designed with the purpose of capturing the some characteristics of the original neutrino, ranging from its initial energy to its ultimate particle products. It's important to note that the more PMT hits information we acquire from a particle, the more accurate its reconstruction becomes.

Since the detector is a 3 dimensional structure, and the particles can travel across the volume in any direction. There are five positional coordinates that determine the trajectory of the particle: x , y , z , θ and ϕ , being x , y , z the spatial coordinates, θ the zenith angle and ϕ the azimuthal angle. As a rough estimate we assume that we need 5 DOM hits to be able to reconstruct with a reasonable accuracy.

With respect to this, we implemented a 5 DOMs hit prerequisite for all events simulated. If the event did not satisfy that condition it is thrown away. This criterion is a rough estimate as a stand-in for the eventual reconstruction algorithm.

5.4 String Spacing Optimization

The primary aim of this simulation is to determine the optimal geometry that maximizes the number of events detected by the detector. There exist two extremes in this regard. On one end, a smaller detector size leads to the triggering of multiple PMTs in a DOM by nearly all events passing through it, although this approach results in a smaller overall volume covered by the detector. On the other hand, a larger detector volume increases the likelihood of a particle traversing through it, but reduces the number of DOMs that will see the event, especially for cascades thus making it impossible to separate neutrinos from noise.

In this analysis, we will endeavour to discover the most favourable combination between these two extremes, balancing the advantages of event triggering with the extent of detector coverage.

Once there is basic DOM trigger algorithm and a minimum DOM hit requirement, we can implement them in the simulation described in section 4.6, where I generated Neutrinos from 10TeV to 10PeV weighted to an Astrophysical flux of a single power law:

$$\Phi_\nu = \phi \times \left(\frac{E}{100\text{TeV}} \right)^{-\gamma}$$

Where $\phi = (6.7_{-1.1}^{+1.2}) \times 10^{-18} \text{GeV}^{-1} \text{s}^{-1} \text{sr}^{-1} \text{cm}^{-2}$ and $\gamma = 2.50 \pm 0.09$ [69], and an Atmospheric flux modeled with nuflux [66]. The trigger optimization is focused on high energy events starting at 10TeV. In fact, to be more precise, for the case of Muon Neutrinos, we are interested in detecting the muon track of the muon produced at the interaction point. Such muon track should start at 10TeV, but since an injected neutrino can share its initial energy with any of its products, an additional filter of events was implemented so that only muons having 10TeV or higher energies, at the point of closest approach to the detector's centre are kept. This filter guarantees that every event going through the detector is at the desired energy range.

Figure 5.2 shows the counts per year from an Astrophysical and Atmospheric flux of

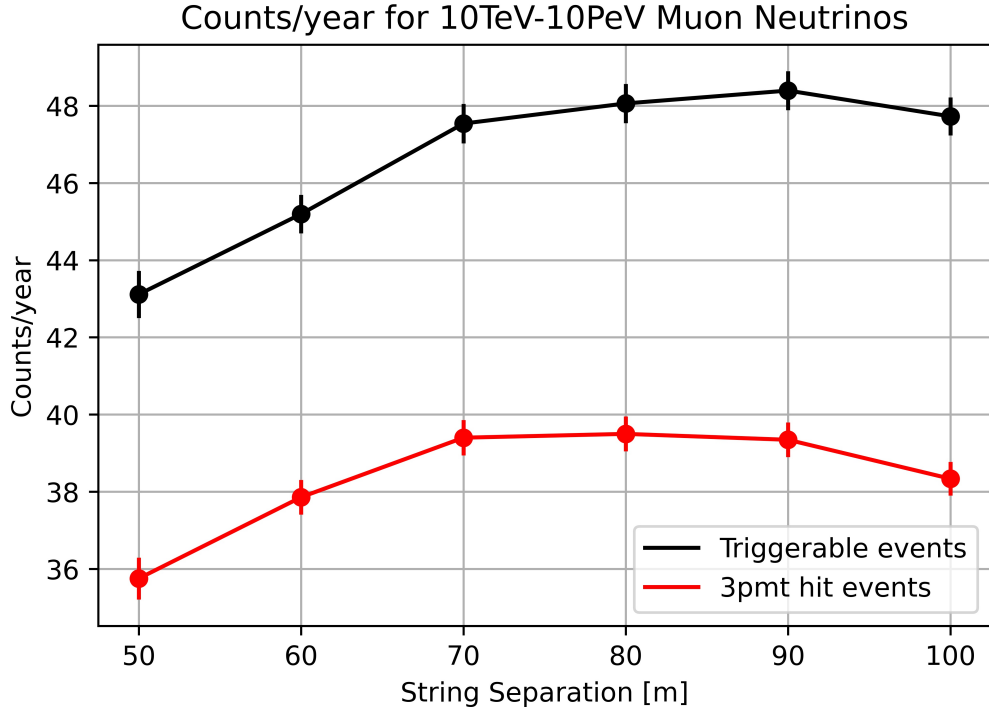


Figure 5.2: Number of events seen per year for 10TeV-10PeV muons weighted to an Astrophysical flux of a single power law, where $\phi = (6.7_{-1.1}^{+1.2}) \times 10^{-18} \text{GeV}^{-1} \text{s}^{-1} \text{sr}^{-1} \text{cm}^{-2}$ and $\gamma = 2.50 \pm 0.09$ [69] and an Atmospheric flux using [66], for different separation distances between strings. The upper line represents the the number of total events that satisfied the reconstructable event condition. The lower line represents the number of events that also hit at least 3 PMTs in a DOM.

Muon Neutrinos from energies starting 10TeV at the point of closest approach to the detector's origin, up to 10PeV. The number of counts measured for reconstructable events increase as the detector volume increases until we get to 100m separation between strings. At that point, the number of events seen starts decreasing. The maximum value is found to be consistent for 70m, 80m, 90m, and 100m due to statistical uncertainties. On the other hand, the second line is the number of events that hit at least 3 PMTs in one DOM. Once again, the highest values remains constant for the 70m, 80m and 90m.

The 80m separation distance geometry was selected because since there is not a significant increase between 70m and 90m, the closer the strings separation the better efficiency there is for cascade detection. In addition to this, there is a significant drop

in counts/year in both curves when going under the 70m mark, so to avoid the edge of the drop, the 80m string separation is the safest selection.

5.5 Mono-Energetic Muon Efficiency

Now that we have a selection for events we consider to be useful for physics, and a geometry optimized for 10TeV particles, we can start looking at efficiencies. This time, instead of injecting muon neutrinos, a new simulation was generated using an isometric source of 10TeV muons. The rationale behind maintaining a mono-energetic sample of 10 TeV is that this energy level serves as the entry point for the range of energies of interest in the project. Muons with higher energies usually deposit more light on the detector modules, which inherently makes us more efficient in detecting higher energy events compared to lower ones. Consequently, this analysis will exclusively concentrate on 10 TeV muons.

From the DOM Trigger algorithm we get the coincidence windows for each DOM in all events. Now is turn to implement a detector trigger and get an efficiency estimation for all events. There were two methods that were explored for this thesis, a PMT rate cutoff, and an adaptive trigger. Both will be explained in this section.

5.5.1 PMT Rate Cutoff

From section 5.1 we noticed that in order for the average single DOM rate to be under 40Hz, we need to trigger the detector, with at least one DOM with a 3 PMT hit coincidence so that the background rate does not saturate the maximum bandwidth. Moreover, since even with a 3 PMT coincidence the single DOM rate can still go over the limit, as figure 5.1 show, the decision made was to set a rate limit on the PMT so that the average single DOM rate will never go over the 8000Hz limit of the detector.

To get the overall efficiency of a sample of events, we take the average of the calculated probability of triggering on a particular event comparing the number of PMT hits it had across all DOMs, with the fraction of time any PMT will be facing

dead time due to the probability of encountering a high rate of bioluminescence that would force shutting down the PMT.

$$P(r)_t = 1 - \prod^N [(1 - t_f(r)) \times combs] \quad (5.3)$$

$$combs = \frac{1}{nCm(16, n_c)} \times \sum_{m=0}^n nCm(8, m) \times nCm(8, n_c - m) \quad (5.4)$$

Equation 5.3 is the derived equation to calculate the probability of triggering on an event at any rate (r). The product is the multiplication of the probabilities of **not** triggering on a DOM, where N is the number of DOMs hit, t_f is the fraction of time a DOM can be at that rate or lower and $combs$ is the fraction of arrangements where there are n_c PMT hits on the non-bioluminescent side. The $combs$ term depends on n_c , the number of PMTs hit in the DOM and n is the minimum number of PMT hits expected to trigger the event. To calculate $combs$ we need to sum over all possible combinations of having n PMTs in the non-bioluminescent side, divided over the total number of combinations of having n_c PMT hits in 16 PMTs. If $n = n_c$, then $combs = 1$, but if n_c is greater than n , the fraction of arrangements is smaller, making it less likely to **not** trigger on that DOM.

Notice that the result of the product is the probability of **not** triggering on an event. So one minus this is the probability of triggering on an event. The reason the function starts as the probability of not triggering a DOM is because it avoids the need to consider all possible combinations of picking DOMs hit out of 200. This way, if there is a DOM hit, there is only one possible combination where no DOMs were hit, but if there is a second DOM hit, now there is only one combination where no DOMs were hit out of the 199 remaining, hence the product of probabilities of **not** triggering.

In order to get back the probability of triggering on the event, you just need to subtract $1 - P(not_triggering)$, as shown in equation 5.3.

For the particular case where $n_c = 4$ and the minimum number of PMT hits needed for trigger is 3 ($n = 3$), then equation 5.4 turns to equation 5.5.

$$combs = \frac{1}{nCm(16, 4)} \times \sum_{m=0}^3 nCm(8, m) \times nCm(8, 4 - m) \quad (5.5)$$

Solving the equation:

$$combs = \frac{1}{1820} \times (70 + 448 + 784 + 448) = \frac{1750}{1820} \approx 0.96$$

Thus, the probability of **not** triggering on that DOM decreases. On the contrary, if n_c is lower than n , then it is not considered for triggering.

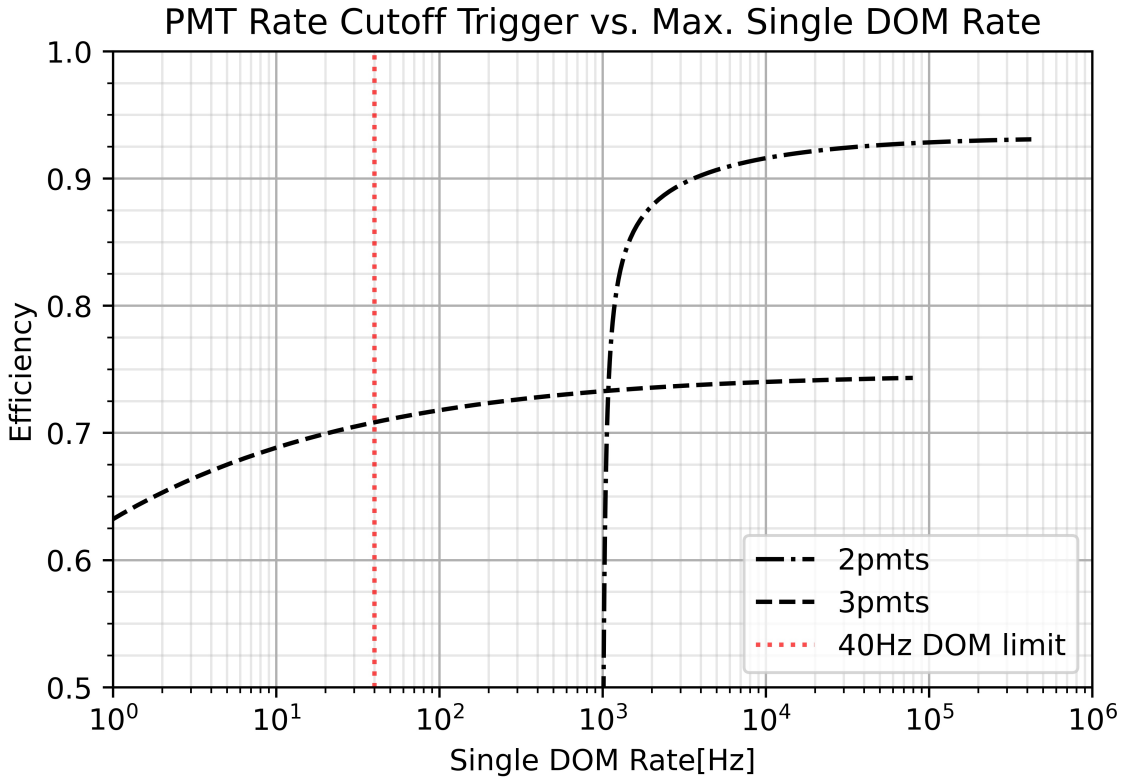


Figure 5.3: Efficiency response depending on the maximum single DOM average rate permitted by limiting the rate on each individual DOM. The dashed line represents the response for 3 PMT hits in a DOM, whereas the dotted line represents the efficiency for 2 PMT hits.

Figure 5.3 shows the estimated efficiency for a 3 PMT coincidence trigger. It yielded a 71% efficiency, considering the 40Hz single DOM average rate limit. At the same time we see that the efficiency line is not steep for those selected rate regions,

that means that we can reduce our limits per DOM a bit, and still get a close to 70% efficiency. This plot also tells us that even at high DOM rates, the efficiency does not go over 75% mark for a 3 PMT trigger. On the other hand, the 2 PMT line shows a higher efficiency but at rates higher than the detector limit. This curve is added for better understanding of the Adaptive trigger; that will come next. A higher number of PMT coincidences would mean lower than 70% in efficiency so it is not being considered for this trigger.

5.5.2 Adaptive Trigger

The main downside from the PMT rate cutoff trigger, is that a fraction of the time, each PMT will be disabled by high rate bioluminescence and so a trigger will be missed reducing the overall efficiency of the trigger.

There is an alternative trigger mechanism developed to trigger each DOM. It is called the adaptive trigger because the number of PMT hits required to trigger the DOM is adaptive to the amount of bioluminescence being registered at the moment. That means that in order to always be below the 40Hz limit DOM rate, the DOM will switch up or down the number of PMTs needed to trigger. For instance, if the single DOM average rate is currently at 40Hz, then the trigger condition can be met at 3 PMT hits as seen above, but if suddenly there is a large bioluminescent event and increases the rate drastically, the DOM will now require 4, 5, or even 6 PMT hits in that DOM so that the single DOM rate limit is being respected. This method guarantees a close to 0% dead time of the detector, at the expense of a drop in efficiency due to an increased level of coincidence.

As we can see from figure 5.4, at 40Hz average single DOM rate, the fraction of time we are under that limit is 91% for 3 PMT hits, so so for the other 9% of the time the trigger will increase the number of PMTs in coincidence required to generate a trigger. With a 4 PMT coincidence the detector is under the limit for over 95% of the time. And for that remaining 5%, there is the fraction of time of triggering on

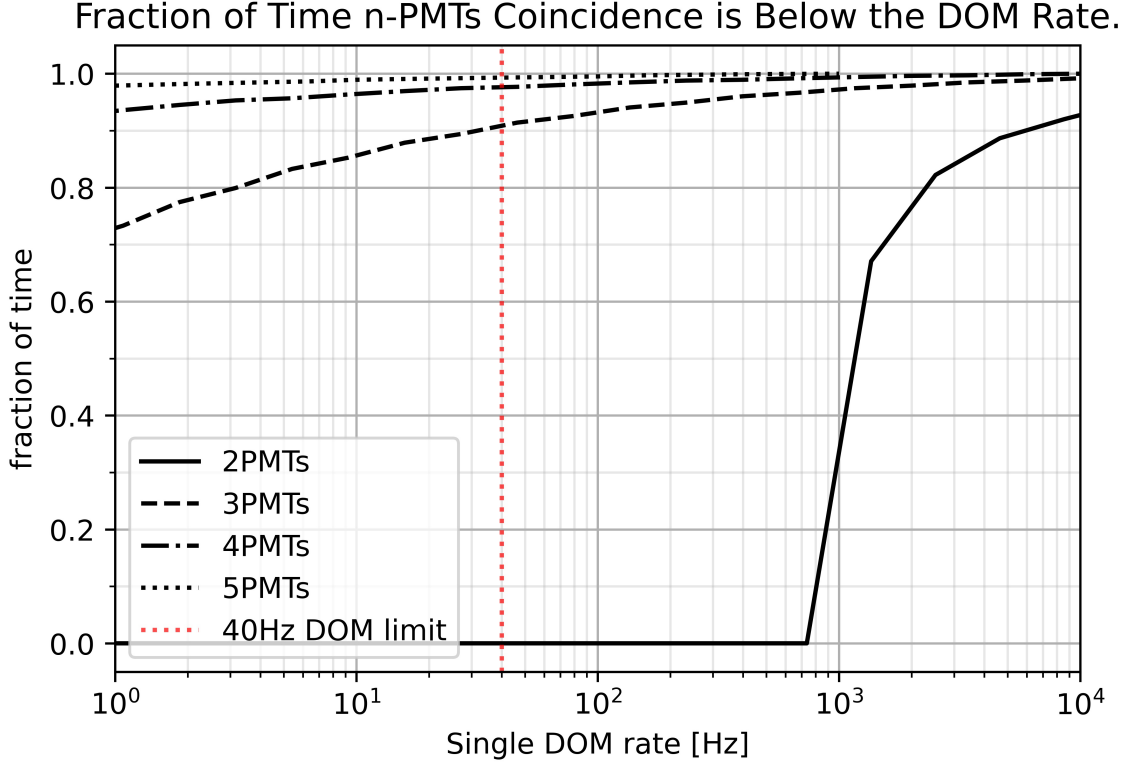


Figure 5.4: Fraction of time a certain n -PMT coincidence in a DOM is below the corresponding single DOM rate limit bin. For the 2PMT case, due to the $k40$ decays, it will never be below the 1kHz rate, so the fraction of the time it is below that mark is 0%.

5PMTs to get 100%. This is how the adaptability of this trigger works.

Just like with the PMT rate cutoff trigger, we derived a probability function of triggering on a particular event. Once again, we start from the probability of not triggering on the event in order to deal with all the DOM combinations as explained earlier in section 5.5.1.

$$P_t(r) = 1 - \prod_{i=1}^N (1 - t_f(n, r)) \quad (5.6)$$

Equation 5.6 is the function obtained. The product represents the probability of not triggering on the event. Each element of the product is the probability of not triggering on a DOM, where N is the number of DOMs hit. The $t_f(n, r)$ is fraction of time at which our event can be triggerable depending on the number of PMT hits

in a DOM and the rate of bioluminescence.

Equation 5.7 shows an example of 4 PMT hits in a DOM, some fraction of the time the DOM can trigger with 3 PMTs only as shown in figure 5.4, some other time at 4 PMTs, and the rest at 5 PMTs, but if the DOM had only 4 hits, that last fraction of time, cannot be triggered. So the $t_f(n, r)$ depends on the number of PMT hits in the DOM; n .

$$P(\text{not_triggering}) = 1 - [t_f(3, 40\text{Hz}) + (t_f(4, 40\text{Hz}) - t_f(4, 40\text{Hz}))] \quad (5.7)$$

Substituting the values from figure 5.4 at 40Hz to equation 5.7, we get:

$$P(\text{not_triggering}) = 1 - [0.90 + (0.95 - 0.90)] = 1 - [0.90 + 0.05] = 0.05$$

From the previous result we obtained the probability of not triggering on a 4PMT coincidence DOM is only 5%. The probabilities of triggering are calculated per event and the statistical mean is obtained for all events, resulting in the efficiency as a function of the rate allowed on each DOM. The adaptive and the PMT rate cutoff trigger plotted together is shown in figure 5.5.

As we can see from figure 5.5, the efficiency response curve follows that of the 2 PMTs and 3 PMTs really closely, there are indeed some regions where the adaptive trigger has a significantly higher efficiency, but the single DOM rate at those levels is well below the maximum rate that we estimate we can readout the detector with. On the other hand we see that the maximum measured efficiencies at higher rates, closely matches the one obtained by the simple PMT rate cutoff trigger at the 2 PMTs coincidence, gaining minimal additional efficiency from the adaptive trigger. However, the region of interest for this detector setup is around the 40Hz area.

The main takeaway from this plot is that the apparent advantage of the adaptive trigger in terms of efficiency at 40Hz is approximately 3%. This boost in efficiency is not large enough to justify the implementation of the adaptive trigger algorithm since it is a lot more complex than the PMT rate cutoff one.

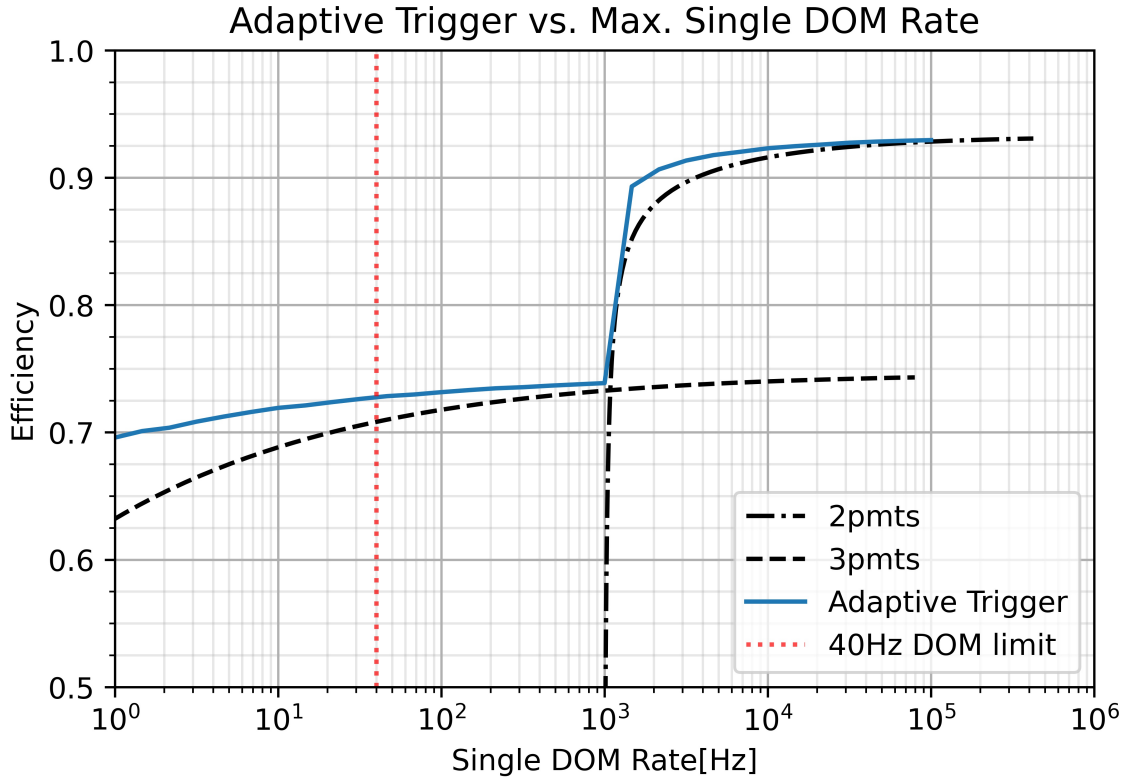


Figure 5.5: Efficiency response depending on the maximum single DOM average rate permitted by adapting the number of PMT hits required to trigger the DOM. The solid line represents the adaptive trigger response at all rates. The dashed line represents the response for 3 PMT hits in a DOM, whereas the dotted line represents the efficiency for 2 PMT hits.

5.5.3 True Efficiency

One notable drawback from both mechanisms was the potential occurrence of dead time for the DOMs, as the current rate across the DOM exceeds a level that can be reliably triggered. The rate set per DOM corresponds to the average DOM rate. Therefore, for an average DOM rate of 40Hz, it implies that the DOM exceeds the specified limit at certain intervals. Consequently, it is crucial to assess the detector's resulting efficiency while taking into account the effects of dead time in the calculations. In reality, there will be a certain level of latency and buffering flexibility that compensates for the effects of exceeding the limit for a specific duration. However, as of the writing of this thesis, the buffer has not been determined, so we are taking

the conservative approach of implementing a hard cutoff at 40Hz.

In order to calculate the fraction of the time the detector would be over the limit, I generated a random sampling of 200 DOMs from a probability function of triggering on a DOM. From the STRAW data we can obtain the time fraction for each DOM at a specific rate, so instead of taking the average at a certain rate, we consider the whole spectrum and randomly pick a rate from that spectrum 200 times. In some cases, a particular DOM will be over the limit, but the rest of the detector might be under the limit, so the overall detector rate is under the maximum capacity. For the particular case of having a 40Hz DOM limit, that translates into a 8000Hz detector limit, which is our estimated readout rate; the fraction of time we are under the limit is 92% as figure 5.6 show. An additional test was made using a DOM limit of 29Hz, and in that case, the detector is under the limit 99% of the time.

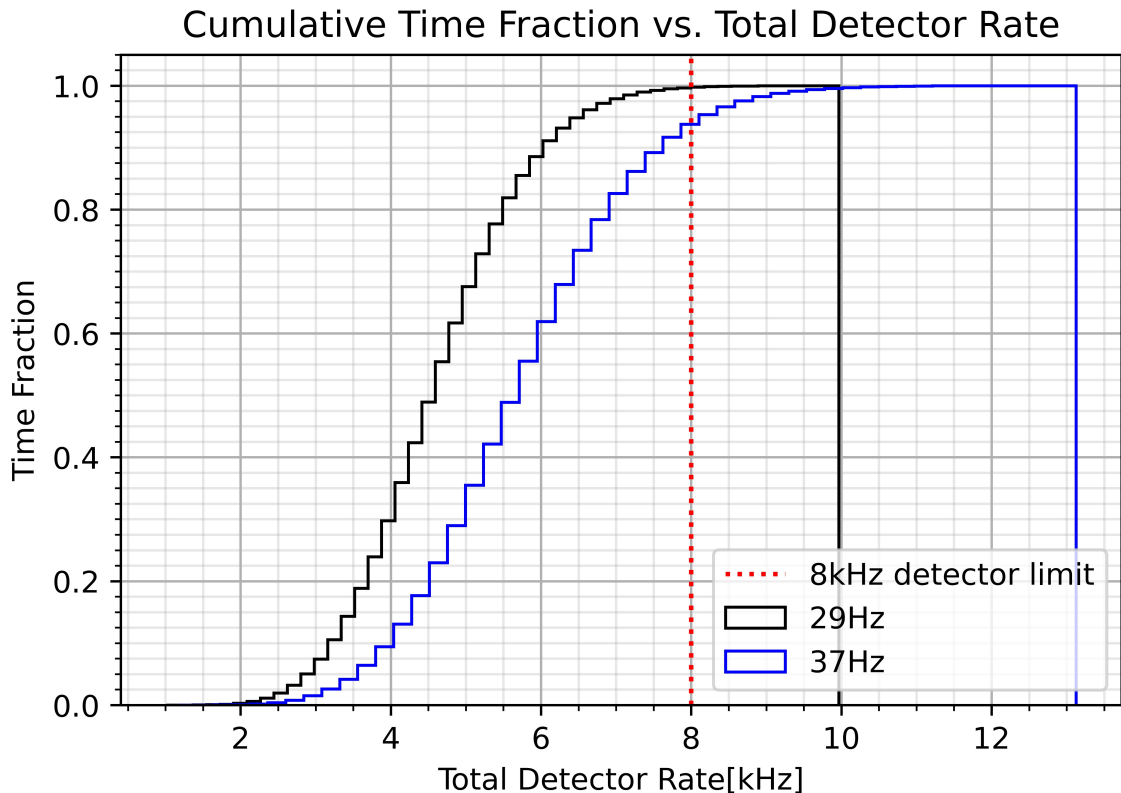


Figure 5.6: Fraction of time the detector rate is under the 8kHz limit when the DOM rate limit is set to 29Hz and 37Hz respectively.

The dead time calculations have a direct impact on the efficiency shown in figure 5.5, when properly scaled to the amount of time the detector will be offline, we notice that the 37Hz limit loses 8% of efficiency with respect of the original value, and almost 6% with compared to the adaptive trigger as shown in figure 5.7. Nevertheless, if the DOM limit is instead then set to 29Hz, allowing the detector limit to still be 8000Hz, almost a 100% of the time the detector is online. This has almost no effect in the overall efficiency. From this we can conclude that the concern of the dead time can be simply solved by limiting the DOM rate to a 29Hz average rate, instead of the 40Hz originally estimated, because the effect on the efficiency is negligible. We avoid having dead time and we keep the simple algorithm implementation for essentially the same efficiency.

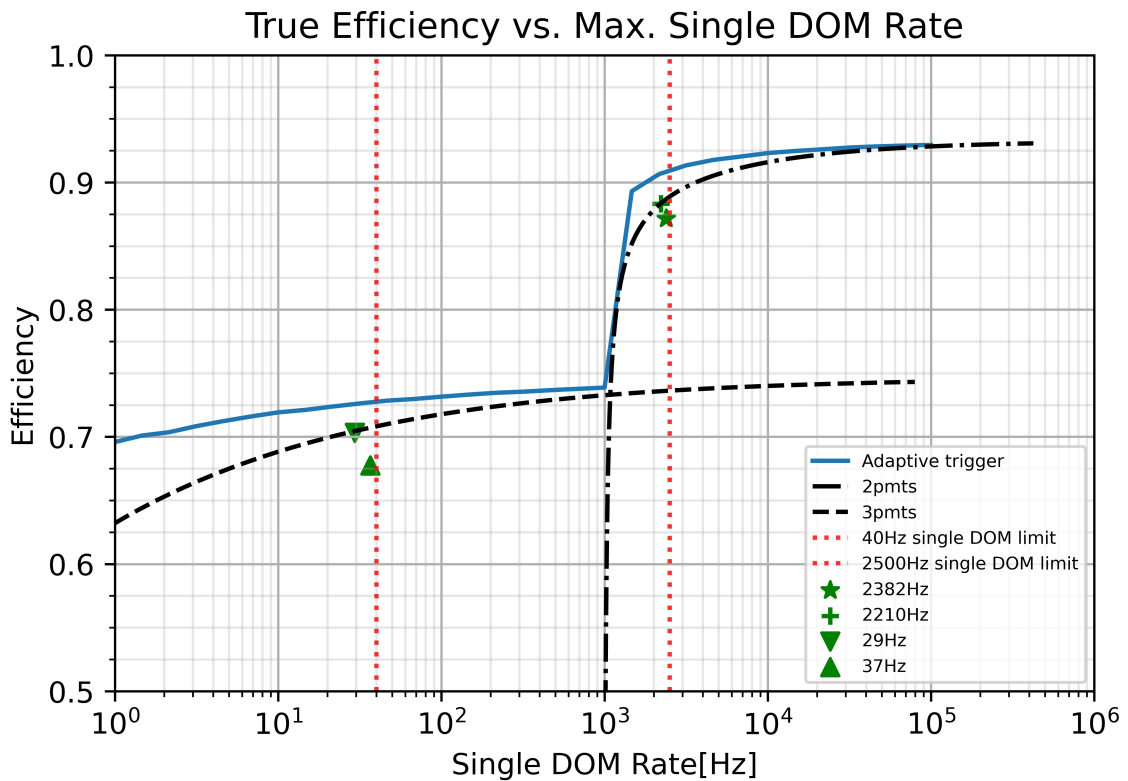


Figure 5.7: Efficiency response when the detector rate is set to 29Hz and 37Hz respectively per DOM.

Another important takeaway from figure 5.7, is that to significantly increase efficiency we need to be able to handle a 2kHz single DOM rate for triggering events.

The evident step function produced by the ^{40}K decays show that the improvement on the efficiency for higher rates only becomes significant at two orders of magnitude or greater rates.

To achieve this, we will need to generate a second-level trigger algorithm that determines whether a full detector readout is necessary, thereby enabling high-rate operation, expecting greater than 2kHz average rate per DOM. The development of the second-level trigger algorithm goes beyond the scope of this thesis, but the benefits of having one have been defined on this work.

There are two star markers on figure 5.7 that followed the same analysis done for the 8kHz case. It shows that for a 2.2kHz DOM average rate limit, there is almost no dead time in the detector. This demands a lot more rate to handle, but the reward on efficiency is proportional, now aiming at close to 90% efficiencies for 10TeV muons. Note that that if we go lower than 2kHz we reach the edge of the step function, falling rapidly in efficiency, that is another region that is optimal to avoid.

5.6 Efficiency vs. Neutrino Energies

Up to this point we have settled for a selection of reconstructable events by enforcing a 5 individual DOMs hit requirement, we also imposed a single DOM average rate limit of 29Hz or a PMT rate cutoff of 500kHz shown in figure 5.1. Lastly, we decided on a trigger algorithm for an 80m detector string separation that consists of at least 1 DOM with 3 PMT hits.

Now we can measure the estimated efficiency of having this trigger for actual neutrino events, and observe how efficient we are to them depending on their energies. Section 4.4 explains in detail the setup of the simulation.

5.6.1 Muon Neutrino Efficiency

Let us start with muon neutrinos, where they range from 100GeV to 10PeV with an uniform distribution.

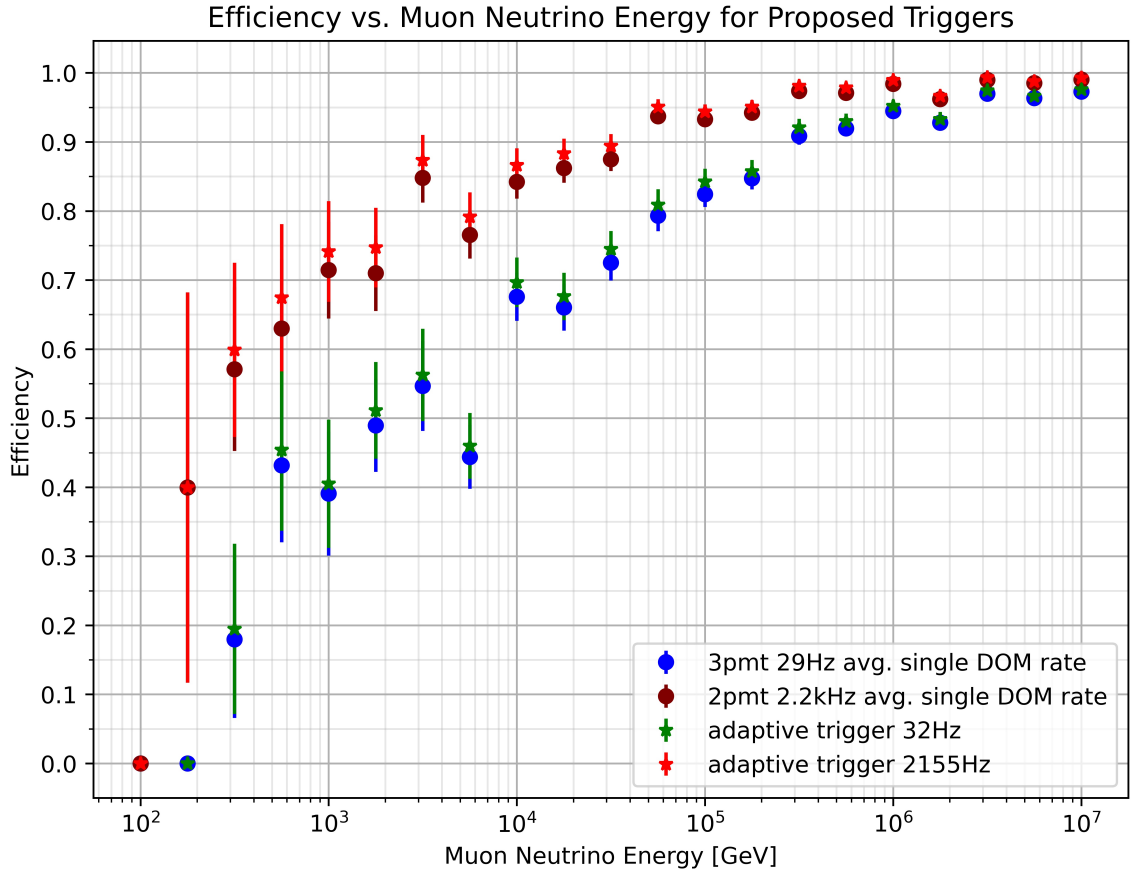


Figure 5.8: Muon neutrino efficiency at different energies. Four different trigger results are shown for comparison. There are split in two main groups: the upper one represents the trigger at 2.2kHz single DOM avg. rate and the lower one at 29Hz. Each group contains the results for the adaptive trigger marked with a star, and the simple trigger result marked with a circle.

If we look at the results shown in figure 5.8, we can see the efficiency of the trigger at detecting muon neutrino events at different energies. In the same figure it is possible to compare both proposed triggers and how much would the efficiency increase if a greater than 2kHz trigger were implemented. For the low rate trigger, both the adaptive and cutoff trigger perform almost identical across all energies, if we pay attention to the 10TeV bin, which is the energy used in section 5.5 for the trigger development, we see that the efficiency at 29Hz remains close to the 70% mark.

Figure 5.8 also demonstrates that the efficiency significantly increases as the energy of the muon rises, eventually reaching an efficiency level very close to 100% for 10PeV

muons, as anticipated. Conversely, there is a rapid decline in efficiency at lower energies. This behaviour was both expected because lower energy events tend to leave less light in the detector, making their detection harder and easier to miss.

Additionally, 5.8 also makes evident the major increase in efficiency if a higher rate trigger is implemented. At the 10TeV bin, the trigger efficiency is estimated to be 85% for both adaptive and cutoff trigger. Moreover, the 100% efficiency reaches a plateau at 1PeV instead of 10PeV for the lower rate trigger.

5.6.2 Electron Neutrino Efficiency

For electron cascade detection we would also expect a high efficiency at high energies because the electron neutrino would generate an electromagnetic cascade after interaction that is heavily dependent on the energy of the neutrino at the point of interaction as seen in section 2.3. The same analysis as the one in section 5.6.1 was repeated for electron neutrinos below.

Figure 5.9 show the efficiency of the detector for triggering electron neutrinos from 100GeV to 10PeV. Taking a closer look at the 10 TeV energy bin for electron neutrinos, akin to our examination of the muon case, reveals that the efficiency for low-rate triggers consistently exceeds 90%. This efficiency steadily climbs until it reaches 100% for higher than 500TeV events. As anticipated, events with energies below 10 TeV exhibit notably lower efficiency until we approach extremely low energy levels, where a 0% efficiency reflects the absence of events meeting the minimum triggering criteria.

However, in this case, the difference between the high-rate trigger and the low-rate trigger is under 10% at 10TeV. This means that for electron neutrinos there is no significant gain in efficiency by increasing the single DOM average rate to 2kHz. A possible explanation to this is that the electromagnetic cascade generation from electron neutrino interaction, emits enough light within the detector volume at 10TeV, to hit multiple PMTs in a DOM, or even multiple DOMs, making it easier to detect

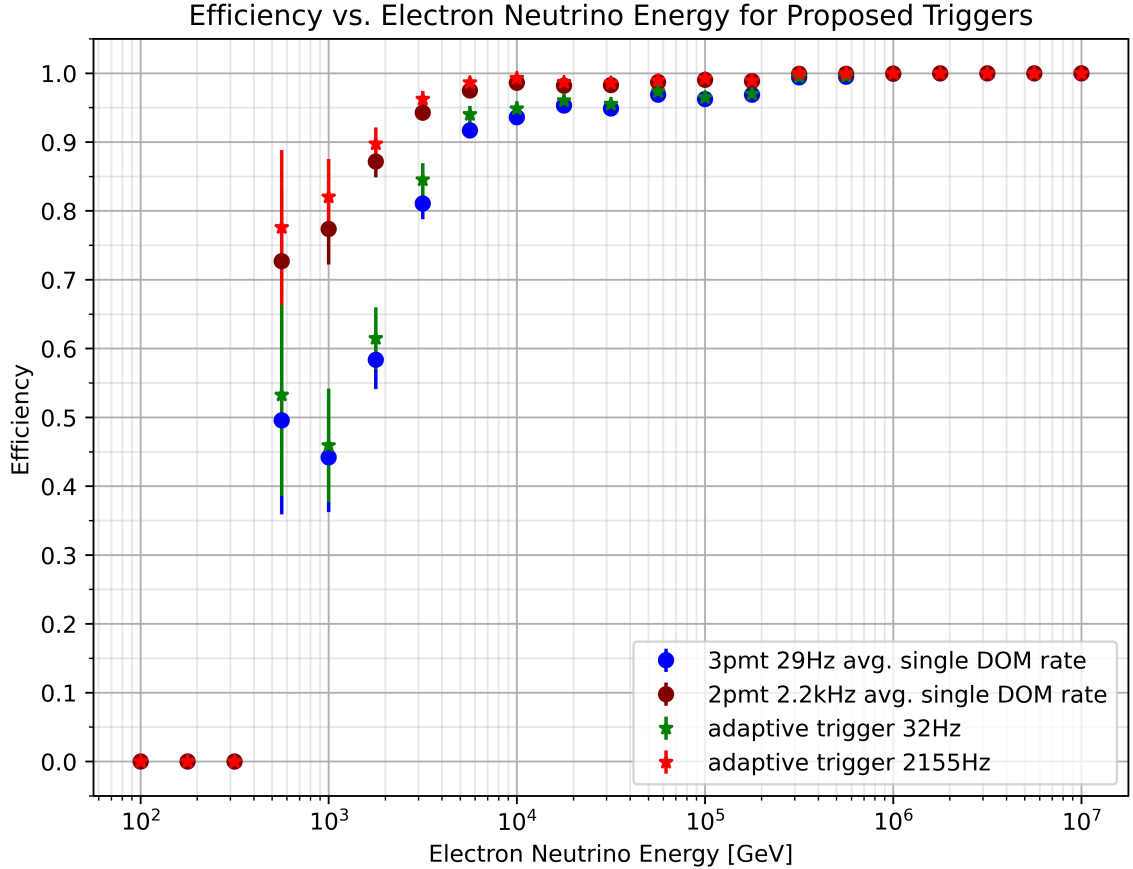


Figure 5.9: Electron neutrino efficiency at different energies. Four different trigger results are shown for comparison. There are split in two main groups: the upper one represent the trigger at 2.2kHz single DOM avg. rate and the lower one at 29Hz. Each group contains the results for the adaptive trigger marked with a star, and the simple trigger result marked with a circle.

than muons, even at low single DOM average rates cut offs.

5.6.3 Tau Neutrino Efficiency

Finally, we can look at tau neutrino events. Similarly to electron neutrino, tau neutrinos produce hadronic cascades, so their detection should not be as efficient as the electron neutrinos', because the attenuation length for hadrons is shorter than photons or electrons given their high interacting probability due to strong force. After running the tau simulation, (see section 4.5.) for tau neutrino events from 100GeV to 10PeV uniformly distributed get the results shown in figure 5.10.

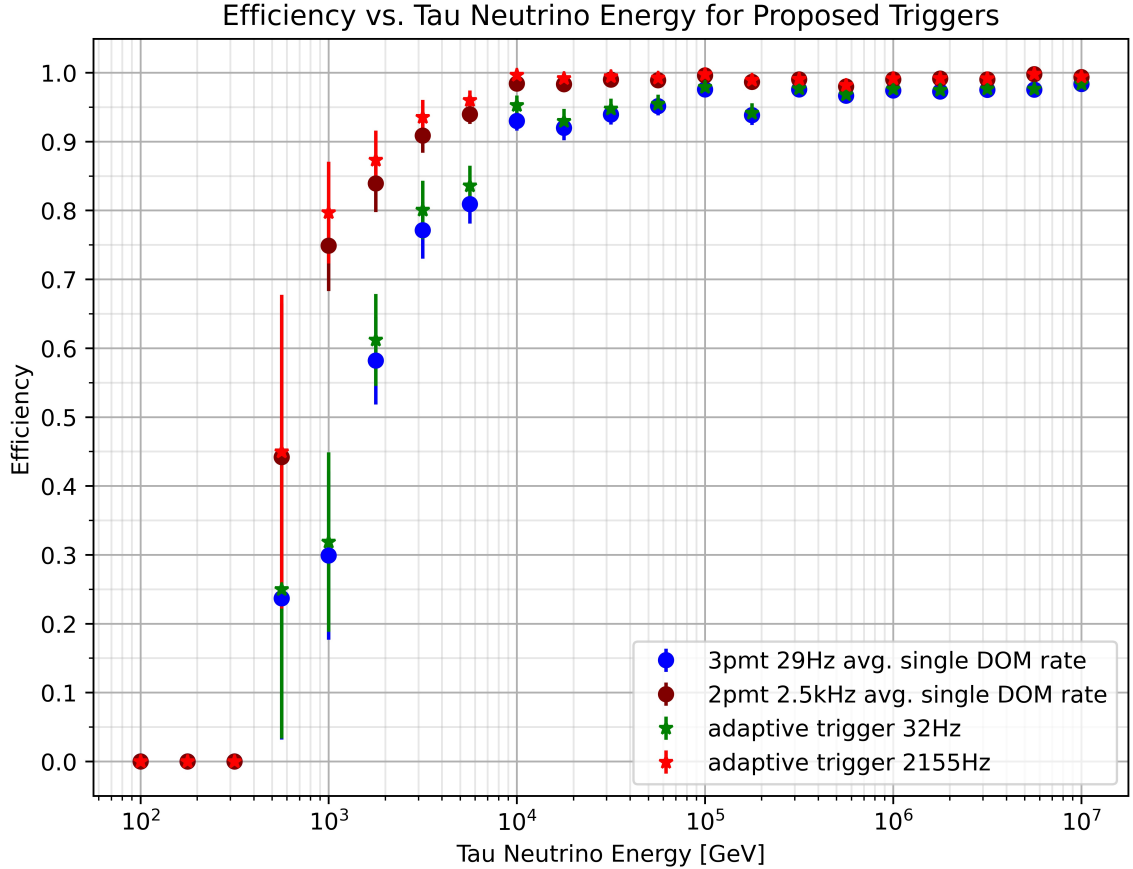


Figure 5.10: Tau neutrino efficiency at different energies. Four different trigger results are shown for comparison. There are split in two main groups: the upper one represent the trigger at 2.2kHz single DOM avg. rate and the lower one at 29Hz. Each group contains the results for the adaptive trigger marked with a star, and the simple trigger result marked with a circle.

Every observed outcome aligns with our expectations. We achieve efficiency levels exceeding 90% for 10 TeV events with the low-rate triggers, and we approach nearly 100% efficiency for events at 10PeV. In contrast to the case of electron neutrinos, where they reach 100% at 1PeV, tau neutrinos plateau at approximately 97% at 100TeV for the low-rate trigger. Although the energy dependence seem similar to the electron neutrino's, the overall efficiency is slightly worse at all energies, with the exception of the high-rate trigger, where the 100% efficiency is achieved at the 10TeV bin, just like in the electron neutrino plot. Moreover, as witnessed in the case of electron neutrinos, events with lower than 500GeV do not trigger the detector due to

their failure to meet the minimum requirements for a triggerable event. This is why they consistently exhibit a flat 0% efficiency.

Despite the better performance of the high-rate trigger, the low-rate one also demonstrates a much higher efficiency detecting tau neutrinos than muon neutrinos. The explanation is analogous to the electron neutrino case, where the 'bubble' of light described in section 2.5, attributed to the hadronic cascade, is easier to detect than a muon track thanks to the increase light emission from the neutrino energy at the point of interaction and the surrounding DOMs, with the caveat of hadrons having a shorter attenuation length than electromagnetic cascades; this drawback is evident in the efficiency difference of 3% of electron and tau neutrino at the plateau region. Another thing to consider is that sometimes a tau neutrino can generate a hadronic cascade and a tau track that then generates a second hadronic cascade: the *double bang*, as covered in section 3.4. The difference in efficiencies from tau and electron neutrino might not be due to the hadronic cascade having a shorter attenuation length, but due to the lower efficiency for detecting muon tracks plus the last *bang* having less energy than the first one because of all the energy lost in the previous interactions.

Overall the high-rate trigger proved to be the best performing trigger for all three neutrino flavours. Even though for electron and tau neutrinos the improved efficiency is only within 5%, for muon neutrinos signifies a much higher increment of 15% at 10TeV and prevailing above the low-rate trigger by over 10%, up to 200TeV.

Chapter 6

Conclusions

The analysis presented in this work provides a detailed examination of the efficiency of the selected trigger algorithms in detecting neutrino events across different energy ranges and flavours. The study focused on muon, electron, and tau neutrinos, considering their distinct interaction characteristics within the P-ONE detector.

The adoption of a 3 PMT hit coincidence trigger in a DOM, with a PMT rate cutoff at 500kHz to account for varying bioluminescent conditions, emerged as the most effective approach, because of its simplicity compared to the adaptive trigger and because it can work with the current detector constraints.

The analysis on muon neutrinos unveiled two trigger scenarios: the low-rate trigger that works with the current detector limitations and yields a 70% efficiency for 10TeV events, and the high-rate trigger that increases the efficiency up to 90%, but it goes beyond the current detector capabilities. Therefore, a global trigger algorithm is needed to reduce the data readout by a factor of 50 if we want to achieve the 15% efficiency improvement.

The subsequent exploration to electron and tau neutrinos showed similar results, demonstrating that the difference between low-rate and high-rate triggers was minimal, suggesting that even at lower rates, electron and tau neutrinos yielded efficiencies of 90% for 10 TeV events and approached 100% for energies beyond 500 TeV.

The overarching theme of the analysis highlights the efficacy of the high-rate trig-

ger across all three neutrino flavours. While muon neutrinos experienced the most significant efficiency improvement, electron and tau neutrinos also benefited from the high-rate trigger mechanism.

In conclusion, we can keep the initial simple low-rate trigger, in spite of the limited efficiency for muon neutrinos because it works fine for electron and tau neutrinos, and due to the simplicity of its implementation. Additionally there is the need to investigate a global detector trigger, that by suppressing readout data, it would allow the implementation of the high-rate trigger in order to increase the efficiency of muon neutrinos at 10TeV to 85% and increase it even more for electron and tau neutrinos. Comparatively, instead of developing another algorithm, these results may prove enough motivation to increase the bandwidth on the detector hardware, allowing for higher-rate triggers. This upgrades would need to be implemented to the inter-DOM connections and to the connections from the mini-junction box to the cluster junction box, in order to increase the overall detector bandwidth.

Furthermore, this results shown are highly sensitive to the bioluminescence model, and the state of the current model is based on assumptions that need to be tested on the P-ONE environment, such as the correlation between DOMs and the bioluminescence due to the turbulence created from the string and the sea currents. The first P-ONE string is expected to be deployed in 2025, allowing to collect new bioluminescence data that will improve the model we are using for estimations. As the number of strings increases, even more complex sources of bioluminescence can be investigated, like the turbulence created from one string, affecting neighbouring strings. This iterative process will enhance our comprehension of how bioluminescence behaves in the specific experimental conditions, enabling further optimization of trigger algorithms and improving overall detector efficiency.

Looking ahead, the implementation of the high-rate trigger stands out as a promising avenue for further exploration. The significant efficiency gains observed across different neutrino flavours, especially in the challenging energy range of 10 TeV un-

underscore the potential benefits of adopting a high-rate trigger mechanism. It could also increase the efficiency for lower than 10TeV neutrinos, allowing for a significantly larger statistics of detected events, because most of the events will be under 10TeV according to our weighted flux. (See figure 4.2) Future work should focus on refining and fine-tuning the high-rate trigger algorithm and bioluminescence model. The continuous evolution of trigger algorithms remains integral to unlocking the full potential of P-ONE and pushing the boundaries of neutrino research.

The current state of the P-ONE detector progresses towards the deployment of the funded first string of the detector in 2025. Furthermore, there are plans for increasing the infrastructure bandwidth by 100 times for the full 70-string detector. This upgrade would facilitate the implementation of a high-rate trigger due to the two orders of magnitude increase in the overall bandwidth.

Bibliography

- [1] IceCube, “Evidence for high-energy extraterrestrial neutrinos at the icecube detector,” *Science*, vol. 342, no. 6161, p. 1 242 856, 2013.
- [2] M. Aartsen *et al.*, “Neutrino emission from the direction of the blazar txs 0506+056 prior to the icecube-170922a alert,” *Science*, vol. 361, no. 6398, pp. 147–151, 2018.
- [3] IceCube and R. A. et al., “Evidence for neutrino emission from the nearby active galaxy ngc 1068,” *Science*, vol. 378, no. 6619, pp. 538–543, 2022. DOI: 10.1126/science.abg3395. eprint: <https://www.science.org/doi/pdf/10.1126/science.abg3395>. [Online]. Available: <https://www.science.org/doi/abs/10.1126/science.abg3395>.
- [4] S. Weinberg, “Conceptual foundations of the unified theory of weak and electromagnetic interactions,” *Reviews of Modern Physics*, vol. 52, no. 3, p. 515, 1980.
- [5] S. Mukhi and P. Roy, “Developments in high energy theory,” *Pramana - Journal of Physics*, vol. 73, May 2009. DOI: 10.1007/s12043-009-0093-9.
- [6] F. Reines and C. L. Cowan Jr, “Free antineutrino absorption cross section. i. measurement of the free antineutrino absorption cross section by protons,” *Physical Review*, vol. 113, no. 1, p. 273, 1959.
- [7] M. Aartsen *et al.*, “Probing the origin of cosmic rays with extremely high energy neutrinos using the icecube observatory,” *Physical Review D*, vol. 88, no. 11, p. 112 008, 2013.
- [8] D. Griffiths, *Introduction to elementary particles*. John Wiley & Sons, 2020.
- [9] R. Davis Jr, D. S. Harmer, and K. C. Hoffman, “Search for neutrinos from the sun,” *Physical Review Letters*, vol. 20, no. 21, p. 1205, 1968.
- [10] Q. Ahmad, R. Allen, T. Andersen, J. Anglin, G Buhler, *et al.*, “Measurement of the rate of $\nu e + d \rightarrow p + p + e^-$ interactions produced by 8b solar neutrinos at the sudbury neutrino observatory,” *Phys. Rev. Lett.*, vol. 87, p. 071 301, 2001.
- [11] S Fukuda *et al.*, “Solar b 8 and hep neutrino measurements from 1258 days of super-kamiokande data,” *Physical Review Letters*, vol. 86, no. 25, p. 5651, 2001.
- [12] Q. R. Ahmad *et al.*, “Direct evidence for neutrino flavor transformation from neutral-current interactions in the sudbury neutrino observatory,” *Physical review letters*, vol. 89, no. 1, p. 011 301, 2002.

- [13] W. C. Haxton and B. R. Holstein, “Neutrino physics,” *American Journal of Physics*, vol. 68, no. 1, pp. 15–32, 2000.
- [14] J. Wolf, K. Collaboration, *et al.*, “The katrin neutrino mass experiment,” *Nuclear Instruments and Methods in Physics Research Section A: Accelerators, Spectrometers, Detectors and Associated Equipment*, vol. 623, no. 1, pp. 442–444, 2010.
- [15] U. F. Katz and C. Spiering, “High-energy neutrino astrophysics: Status and perspectives,” *Progress in Particle and Nuclear Physics*, vol. 67, no. 3, pp. 651–704, 2012.
- [16] J. A. Formaggio and G. P. Zeller, “From ν_e to $\bar{\nu}_e$: Neutrino cross sections across energy scales,” *Reviews of Modern Physics*, vol. 84, no. 3, 1307–1341, Sep. 2012, ISSN: 1539-0756. DOI: 10.1103/revmodphys.84.1307. [Online]. Available: <http://dx.doi.org/10.1103/RevModPhys.84.1307>.
- [17] M. A. *et al.*, “The IceCube neutrino observatory: Instrumentation and online systems,” *Journal of Instrumentation*, vol. 12, no. 03, P03012–P03012, 2017. DOI: 10.1088/1748-0221/12/03/p03012. [Online]. Available: <https://doi.org/10.1088%2F1748-0221%2F12%2F03%2Fp03012>.
- [18] [Online]. Available: <https://icecube.wisc.edu/>.
- [19] *Km3net gallery*, 2023. [Online]. Available: <https://www.km3net.org/pictures-and-videos/>.
- [20] Y. Fukuda *et al.*, “The Super-Kamiokande detector,” *Nucl. Instrum. Meth. A*, vol. 501, V. A. Ilyin, V. V. Korenkov, and D. Perret-Gallix, Eds., pp. 418–462, 2003. DOI: 10.1016/S0168-9002(03)00425-X.
- [21] *Snolab*, 2023. [Online]. Available: <https://www.snolab.ca/>.
- [22] T. K. Gaisser, R. Engel, and E. Resconi, “Atmospheric muons and neutrinos,” in *Cosmic Rays and Particle Physics*, 2nd ed. Cambridge University Press, 2016, 126–148. DOI: 10.1017/CBO9781139192194.008.
- [23] P. Cerenkov *et al.*, “Visible emission of clean liquids by action of γ radiation,” *Dok Akad Nauk SSSR*, vol. 2, pp. 451–454, 1934.
- [24] I. Tamm and I. Frank, “Coherent radiation of fast electrons in a medium,” in *Dokl. Akad. Nauk SSSR*, vol. 14, 1937, pp. 107–112.
- [25] U. Katz, “Cherenkov light imaging in astroparticle physics,” *Nuclear Instruments and Methods in Physics Research Section A: Accelerators, Spectrometers, Detectors and Associated Equipment*, vol. 952, p. 161 654, 2020.
- [26] J. Boger *et al.*, “The sudbury neutrino observatory,” *Nuclear Instruments and Methods in Physics Research Section A: Accelerators, Spectrometers, Detectors and Associated Equipment*, vol. 449, no. 1-2, pp. 172–207, 2000.

- [27] C. Spiering, “Neutrino detectors under water and ice,” in *Particle Physics Reference Library: Volume 2: Detectors for Particles and Radiation*, C. W. Fabjan and H. Schopper, Eds. Cham: Springer International Publishing, 2020, pp. 785–822, ISBN: 978-3-030-35318-6. DOI: 10.1007/978-3-030-35318-6_17. [Online]. Available: https://doi.org/10.1007/978-3-030-35318-6_17.
- [28] *Pacific ocean neutrino experiment-website*. [Online]. Available: <https://www.pacific-neutrino.org/>.
- [29] M. Agostini *et al.*, “The pacific ocean neutrino experiment,” *Nature Astronomy*, vol. 4, no. 10, pp. 913–915, 2020.
- [30] M. G. Aartsen *et al.*, “First observation of pev-energy neutrinos with icecube,” *Physical review letters*, vol. 111, no. 2, p. 021 103, 2013.
- [31] M. Ahlers and F. Halzen, “High-energy cosmic neutrino puzzle: A review,” *Reports on Progress in Physics*, vol. 78, no. 12, p. 126 901, 2015.
- [32] *Ocean networks canada*. [Online]. Available: <https://www.oceannetworks.ca/>.
- [33] N. Bailly *et al.*, “Two-year optical site characterization for the pacific ocean neutrino experiment (p-one) in the cascadia basin,” *The European Physical Journal C*, vol. 81, no. 12, p. 1071, 2021.
- [34] M Boehmer *et al.*, “Straw (strings for absorption length in water): Pathfinder for a neutrino telescope in the deep pacific ocean,” *Journal of Instrumentation*, vol. 14, no. 02, P02013, 2019.
- [35] C. Fruck, A. Gärtner, I. C. Rea, and J. Stacho, *Optical analysis of the pacific ocean neutrino experiment (p-one) site using data from the first pathfinder mooring*, 2021.
- [36] N. Bailly *et al.*, “Two-year optical site characterization for the pacific ocean neutrino experiment (p-one) in the cascadia basin,” *The European Physical Journal C*, vol. 81, no. 12, p. 1071, 2021.
- [37] M. A. et al., “ANTARES: The first undersea neutrino telescope,” *Nuclear Instruments and Methods in Physics Research Section A: Accelerators, Spectrometers, Detectors and Associated Equipment*, vol. 656, no. 1, pp. 11–38, 2011. DOI: 10.1016/j.nima.2011.06.103. [Online]. Available: <https://doi.org/10.1016%2Fj.nima.2011.06.103>.
- [38] A. Avrorin *et al.*, “High-energy neutrino astronomy and the baikal-gvd neutrino telescope,” *Physics of Atomic Nuclei*, vol. 84, pp. 513–518, 2021.
- [39] J. Carter, R. B. Ickert, D. F. Mark, M. M. Tremblay, A. J. Cresswell, and D. C. Sanderson, “Production of ^{40}Ar by an overlooked mode of ^{40}K decay with implications for ^{40}Ar geochronology,” *Geochronology*, vol. 2, no. 2, pp. 355–365, 2020.
- [40] F Henningsen, “Pacific ocean neutrino experiment: Expected performance of the first cluster of strings,” *PoS ICRC2023*, vol. 1053, 2023.

- [41] F. f. t. P.-O. c. Henningsen, “Pacific ocean neutrino experiment: Expected performance of the first cluster of strings,” *Proceedings of Science*, 2023.
- [42] E. A. Widder, “Bioluminescence in the ocean: Origins of biological, chemical, and ecological diversity,” *Science*, vol. 328, no. 5979, pp. 704–708, 2010.
- [43] S. Martini and S. H. Haddock, “Quantification of bioluminescence from the surface to the deep sea demonstrates its predominance as an ecological trait,” *Scientific reports*, vol. 7, no. 1, p. 45750, 2017.
- [44] E. A. Widder *et al.*, “Bioluminescence in the monterey submarine canyon: Image analysis of video recordings from a midwater submersible,” *Marine Biology*, vol. 100, pp. 541–551, 1989.
- [45] *Icecube collaboration. detecting neutrinos — icecube masterclass*. 2023. [Online]. Available: <https://masterclass.icecube.wisc.edu/de/node/213>.
- [46] C. Spiering, “Neutrino detectors under water and ice: Detectors for special applications,” *Detectors for Particles and Radiation. Part 2: Systems and Applications*, pp. 89–114, 2011.
- [47] D. E. Groom, N. V. Mokhov, and S. I. Striganov, “Muon stopping power and range tables 10 mev–100 tev,” *Atomic Data and Nuclear Data Tables*, vol. 78, no. 2, pp. 183–356, 2001.
- [48] J. S. Useche and C. A. Avila, “Estimation of cosmic-muon flux attenuation by monserrate hill in bogota,” *Journal of Instrumentation*, 2018. [Online]. Available: <https://api.semanticscholar.org/CorpusID:53452267>.
- [49] I. F. M. Albuquerque, J. Lamoureux, and G. F. Smoot, “Astrophysical neutrino event rates and sensitivity for neutrino telescopes,” *The Astrophysical Journal Supplement Series*, vol. 141, no. 1, pp. 195–209, 2002. DOI: 10.1086/340281. [Online]. Available: <https://doi.org/10.1086%2F340281>.
- [50] E. Andres, “The AMANDA neutrino telescope: Principle of operation and first results,” *Astroparticle Physics*, vol. 13, no. 1, pp. 1–20, 2000. DOI: 10.1016/S0927-6505(99)00092-4. [Online]. Available: <https://doi.org/10.1016%2Fs0927-6505%2899%2900092-4>.
- [51] R. Abbasi *et al.*, “The design and performance of icecube deepcore,” *Astroparticle physics*, vol. 35, no. 10, pp. 615–624, 2012.
- [52] A. Ishihara, “The icecube upgrade—design and science goals,” *arXiv preprint arXiv:1908.09441*, 2019.
- [53] R. Abbasi *et al.*, “Design and performance of the multi-pmt optical module for icecube upgrade,” *ICRC2021*, 2021.
- [54] U. F. Katz, “Km3net: Towards a km3 mediterranean neutrino telescope,” *Nuclear Instruments and Methods in Physics Research Section A: Accelerators, Spectrometers, Detectors and Associated Equipment*, vol. 567, no. 2, pp. 457–461, 2006.

- [55] E. Migneco *et al.*, “Status of nemo,” *Nuclear Instruments and Methods in Physics Research Section A: Accelerators, Spectrometers, Detectors and Associated Equipment*, vol. 567, no. 2, pp. 444–451, 2006.
- [56] P. A. Rapidis, N. collaboration, *et al.*, “The nestor underwater neutrino telescope project,” *Nuclear Instruments and Methods in Physics Research Section A: Accelerators, Spectrometers, Detectors and Associated Equipment*, vol. 602, no. 1, pp. 54–57, 2009.
- [57] KM3NeT, *Astroparticle physics with arca*, 2023. [Online]. Available: <https://www.km3net.org/research/physics/astronomy-with-arca/>.
- [58] A. Margiotta, “The km3net infrastructure: Status and first results,” *arXiv preprint arXiv:2208.07370*, 2022.
- [59] KM3NeT, *Astroparticle physics with orca*, 2023. [Online]. Available: <https://www.km3net.org/research/physics/particle-physics-with-orca/>.
- [60] V. Allakhverdyan *et al.*, “Status of the baikal-gvd neutrino telescope and main results,” *Bulletin of the Russian Academy of Sciences: Physics*, pp. 1–4, 2023.
- [61] Y. Malyshkin, B.-G. collaboration, *et al.*, “Baikal-gvd neutrino telescope: Design reference 2022,” *Nuclear Instruments and Methods in Physics Research Section A: Accelerators, Spectrometers, Detectors and Associated Equipment*, vol. 1050, p. 168 117, 2023.
- [62] T. DeYoung, “IceTray: A software framework for IceCube,” in *14th International Conference on Computing in High-Energy and Nuclear Physics*, 2005, pp. 463–466.
- [63] R. Abbasi, M. Ackermann, J. Adams, and J. Aguilar, “LeptonInjector and LeptonWeighter: A neutrino event generator and weighter for neutrino observatories,” *Computer Physics Communications*, vol. 266, p. 108 018, 2021. DOI: 10.1016/j.cpc.2021.108018. [Online]. Available: <https://doi.org/10.1016%2Fj.cpc.2021.108018>.
- [64] J.-H. Koehne *et al.*, “Proposal: A tool for propagation of charged leptons,” *Computer Physics Communications*, vol. 184, no. 9, pp. 2070–2090, 2013, ISSN: 0010-4655. DOI: <https://doi.org/10.1016/j.cpc.2013.04.001>. [Online]. Available: <https://www.sciencedirect.com/science/article/pii/S0010465513001355>.
- [65] K. C., *Clsim*, <https://github.com/claudiok/clsim>, 2019.
- [66] *Nuflux*. [Online]. Available: <https://github.com/icecube/nuflux/tree/main>.
- [67] *Photospline*. [Online]. Available: <https://github.com/icecube/photospline>.
- [68] J. S. Gainer, J. Lykken, K. T. Matchev, S. Mrenna, and M. Park, “Exploring theory space with monte carlo reweighting,” *Journal of High Energy Physics*, vol. 2014, no. 10, Oct. 2014, ISSN: 1029-8479. DOI: 10.1007/jhep10(2014)078. [Online]. Available: [http://dx.doi.org/10.1007/JHEP10\(2014\)078](http://dx.doi.org/10.1007/JHEP10(2014)078).

- [69] M. G. e. a. Aartsen, “A combined maximum-likelihood analysis of the high-energy astrophysical neutrino flux measured with icecube,” *The Astrophysical Journal*, vol. 809, no. 1, p. 98, Aug. 2015, ISSN: 1538-4357. DOI: 10.1088/0004-637x/809/1/98. [Online]. Available: <http://dx.doi.org/10.1088/0004-637X/809/1/98>.

Appendix A: Simulation Output

In chapter 4 the simulation scheme for this analysis was reviewed. The particles were injected, propagated and then they went through a DOM-launching module that would return the trigger pulse map of the event and the properties of the event. These information was the one used for the rest of the analysis. Dataio-Shovel is an IceTray interface that allows for the manipulation of the resulting data of the simulation. Figure A.1 shows an example of a simulation output, where each Q at the bottom of the figure represent an individual event. Each event also displays the list of module outputs of all the modules the particle went through. In the particular case of a muon simulation, the initial properties of the injected muon are stored in the MMCTrackList key, the I3MCTree key contains all the particle interactions the original muon went through on its path, and its remaining energy. The I3Photons key contains all the photons emitted by a particle for that event, it provides the direction of each photon, its wavelength and the time of emission. The Trigger Pulse Map key contains all the hits received by every DOM in all strings by a single event. It also contains the time of hit. The last key was used for developing the trigger strategies.

Figure A.2 shows the MMCTrackList key in the Dataio-Shovel interface. It contains the initial coordinates of the injected muon as well as initial energy. It also contains coordinates and energy at the point of closest approach to the detector's centre and final coordinates and energy of the muon when it goes over the detector's interaction volume. It also provides the total energy lost in the event, the total length of the particle injected, the type of particle, etc.

Figure A.3 shows a fragment of the particle interactions that the initial muon go



Figure A.1: Example of simulated events as seen through the Dataio-Shovel interface. Each Q at the bottom represent a simulated event, and each event shows the information displayed on the figure. From the particle injection properties, to the trigger pulse map, and all of the stages in between.

through for the whole event. The I3MCTree key contains the initial muon’s energy and coordinates and it provides a list of the produced particles with their coordinates and energies. The initial muon is preserved and followed through during the event to keep track of its remaining energy and current location.

Figure A.4 shows an fragment of the simulated photons during a muon event. The I3Photons key contains a list of all photons, their timestamp, coordinates, directions, and produced wavelengths.

Figure A.5 shows a fragment of the trigger pulse map of the simulation after the photon propagation. The trigger pulse map key contains the list of PMT hits on each DOM and on every string. The string number is represented on the first number on the OMKey class variable, and the second number represents the DOM hit in that

```

MMCTrackList [I3Vector<I3MMCTrack>]:
[I3MMCTrack = [
(xi, yi, zi, ti, Ei) = (-116.231 ,29.8405 ,385.985 ,0 ,10000)
(xc, yc, zc, tc, Ec) = (141.882 ,15.6313 ,222.11 ,1020.94 ,9029.37)
(xf, yf, zf, tf, Ef) = (999.535 ,-31.5913 ,-322.346 ,4413.19 ,7391.51)
Elost = 2608.49
Particle = [ I3Particle MajorID : 1396456645571640284
MinorID : 25545
Zenith : 1.00578
Azimuth : 3.0866
X : -116.231
Y : 29.8405
Z : 385.985
Time : 0
Energy : 10000
Speed : 0.299792
Length : 3904.76
Type : MuMinus
PDG encoding : 13
Shape : Null
Status : NotSet
Location : InIce
]]
]

```

Figure A.2: MMCTrackList key of a simulated muon. It contains all the basic information of the injected muon. Initial coordinates and energy, coordinates and energy at the point of closest approach and final coordinates and energy.

string. The width attribute on each hit represent the PMT hit on the DOM.

```

I3MCTree [TreeBase::Tree<I3Particle, I3ParticleID, i3hash<I3ParticleID> >]:
[I3MCTree:
  25544 unknown (-116.231m, 29.8405m, 385.985m) (57.627deg, 176.849deg) 0ns 10000GeV nanm
  25545 MuMinus (-116.231m, 29.8405m, 385.985m) (57.627deg, 176.849deg) 0ns 10000GeV 3904.76m
  25547 MuMinus (-116.231m, 29.8405m, 385.985m) (57.6271deg, 176.849deg) 0ns 10000GeV 3.84082m
  25548 PairProd (-112.992m, 29.6622m, 383.928m) (57.6271deg, 176.849deg) 12.8116ns 356.652GeV 0m
  25549 MuMinus (-112.992m, 29.6622m, 383.928m) (57.627deg, 176.849deg) 12.8116ns 9642.34GeV 2.55293m
  25550 PairProd (-110.839m, 29.5437m, 382.561m) (57.627deg, 176.849deg) 21.3273ns 1.20839GeV 0m
  25551 MuMinus (-110.839m, 29.5437m, 382.561m) (57.6275deg, 176.849deg) 21.3273ns 9640.46GeV 9.29568m
  25552 PairProd (-103m, 29.1122m, 377.584m) (57.6275deg, 176.849deg) 52.3343ns 27.9287GeV 0m
  25553 MuMinus (-103m, 29.1122m, 377.584m) (57.6274deg, 176.849deg) 52.3343ns 9610.1GeV 0.173937m
  25554 PairProd (-102.853m, 29.1041m, 377.491m) (57.6274deg, 176.849deg) 52.9145ns 1.12013GeV 0m
  25555 MuMinus (-102.853m, 29.1041m, 377.491m) (57.6275deg, 176.849deg) 52.9145ns 9608.93GeV 5.03982m
  25556 PairProd (-98.6028m, 28.8702m, 374.793m) (57.6275deg, 176.849deg) 69.7255ns 3.31233GeV 0m
  25557 MuMinus (-98.6028m, 28.8702m, 374.793m) (57.6273deg, 176.849deg) 69.7255ns 9604.3GeV 4.31014m
  25558 PairProd (-94.968m, 28.6701m, 372.485m) (57.6273deg, 176.849deg) 84.1026ns 1.39447GeV 0m
  25559 MuMinus (-94.968m, 28.6701m, 372.485m) (57.6272deg, 176.849deg) 84.1026ns 9601.77GeV 1.46096m
  25560 PairProd (-93.736m, 28.6023m, 371.703m) (57.6272deg, 176.849deg) 88.9759ns 208.567GeV 0m
  25561 MuMinus (-93.736m, 28.6023m, 371.703m) (57.6275deg, 176.85deg) 88.9759ns 9392.82GeV 3.75494m
  25562 PairProd (-90.5694m, 28.428m, 369.692m) (57.6275deg, 176.85deg) 101.501ns 2.33861GeV 0m
  25563 MuMinus (-90.5694m, 28.428m, 369.692m) (57.6273deg, 176.849deg) 101.501ns 9389.5GeV 10.168m
  25564 PairProd (-81.9946m, 27.956m, 364.248m) (57.6273deg, 176.849deg) 135.418ns 3.24678GeV 0m
  25565 MuMinus (-81.9946m, 27.956m, 364.248m) (57.6272deg, 176.849deg) 135.418ns 9383.59GeV 0.558972m
  25566 PairProd (-81.5232m, 27.9301m, 363.949m) (57.6272deg, 176.849deg) 137.282ns 0.946155GeV 0m
  25567 MuMinus (-81.5232m, 27.9301m, 363.949m) (57.6277deg, 176.85deg) 137.282ns 9382.5GeV 4.89234m
  25568 PairProd (-77.3975m, 27.703m, 361.329m) (57.6277deg, 176.85deg) 153.602ns 1.35744GeV 0m
  25569 MuMinus (-77.3975m, 27.703m, 361.329m) (57.6277deg, 176.85deg) 153.602ns 9379.86GeV 2.79645m
  25570 DeltaE (-75.0392m, 27.5732m, 359.832m) (57.6277deg, 176.85deg) 162.929ns 0.531374GeV 0m
  25571 MuMinus (-75.0392m, 27.5732m, 359.832m) (57.6277deg, 176.85deg) 162.929ns 9378.59GeV 5.76903m
  25572 PairProd (-70.1741m, 27.3054m, 356.743m) (57.6277deg, 176.85deg) 182.173ns 0.69293GeV 0m
  25573 MuMinus (-70.1741m, 27.3054m, 356.743m) (57.6274deg, 176.85deg) 182.173ns 9376.39GeV 5.11468m
  25574 PairProd (-65.8609m, 27.068m, 354.005m) (57.6274deg, 176.85deg) 199.234ns 1.05897GeV 0m
  25575 MuMinus (-65.8609m, 27.068m, 354.005m) (57.6274deg, 176.85deg) 199.234ns 9373.99GeV 0.984691m
  25576 PairProd (-65.0305m, 27.0223m, 353.478m) (57.6274deg, 176.85deg) 202.518ns 0.903078GeV 0m
  25577 MuMinus (-65.0305m, 27.0223m, 353.478m) (57.6273deg, 176.85deg) 202.518ns 9372.83GeV 0.629306m
  25578 PairProd (-64.4998m, 26.9931m, 353.141m) (57.6273deg, 176.85deg) 204.617ns 4.65337GeV 0m
  25579 MuMinus (-64.4998m, 26.9931m, 353.141m) (57.627deg, 176.85deg) 204.617ns 9368.01GeV 25.0432m
  25580 PairProd (-43.3807m, 25.8306m, 339.732m) (57.627deg, 176.85deg) 288.153ns 81.1665GeV 0m
  25581 MuMinus (-43.3807m, 25.8306m, 339.732m) (57.6275deg, 176.85deg) 288.153ns 9280.28GeV 4.26379m
  25582 PairProd (-39.785m, 25.6328m, 337.449m) (57.6275deg, 176.85deg) 302.375ns 1.76996GeV 0m

```

Figure A.3: I3MCTree key of a simulated muon. It contains the initial muon's energy and coordinates and it provides a list of the produced particles with their coordinates and energies. The initial muon is preserved and followed through during the event to keep track of its remaining energy and current location.

```

I3Photons [I3Map<ModuleKey, I3Vector<I3CompressedPhoton> >]:
[ModuleKey(1,16) => [[I3CompressedPhoton:
    Time: 949.111
    Weight: 10.6989
    Wavelength: 4.34345e-07
    Zenith: 0.992036
    Azimuth: 1.67247
    Position: (-0.175709,-0.0679665,0.10318)
    Group Vel.: 0.216425
    ParticleID: 1396456645571640284,25598)]],
ModuleKey(2,14) => [[I3CompressedPhoton:
    Time: 1038.91
    Weight: 13.0314
    Wavelength: 4.79411e-07
    Zenith: 0.398583
    Azimuth: 2.93176
    Position: (-0.0413704,-0.0635033,0.202011)
    Group Vel.: 0.217865
    ParticleID: 1396456645571640284,25610)]],
ModuleKey(2,15) => [[I3CompressedPhoton:
    Time: 861.629
    Weight: 11.4501
    Wavelength: 4.53366e-07
    Zenith: 0.872332
    Azimuth: 3.11244
    Position: (0.00561523,0.101368,0.19017)
    Group Vel.: 0.217099
    ParticleID: 1396456645571640284,25610)], [I3CompressedPhoton:
    Time: 820.341
    Weight: 10.1171
    Wavelength: 3.99934e-07
    Zenith: 0.645645
    Azimuth: 4.07944
    Position: (-0.112083,-0.161167,-0.0898743)
    Group Vel.: 0.214871
    ParticleID: 1396456645571640284,25629)]],

```

Figure A.4: The I3Photons key contains a list of all photons, their timestamp, coordinates, directions, and produced wavelengths.

```

triggerpulsemap_nonoise [I3Map<OMKey, vector<I3RecoPulse> >]:
As an I3RecoPulseSeriesMap:
[OMKey(1,16,0) => [[I3RecoPulse:
    Time : 950.796
    Charge : 0.736819
    Width : 12
    Flags :
]],
OMKey(2,14,0) => [[I3RecoPulse:
    Time : 1038.58
    Charge : 1.07251
    Width : 10
    Flags :
]],
OMKey(2,15,0) => [[I3RecoPulse:
    Time : 819.949
    Charge : 0.475566
    Width : 14
    Flags :
], [I3RecoPulse:
    Time : 861.981
    Charge : 1.52398
    Width : 14
    Flags :
]],
OMKey(2,16,0) => [[I3RecoPulse:
    Time : 730.147
    Charge : 2.35904
    Width : 15
    Flags :
]],
OMKey(7,16,0) => [[I3RecoPulse:
    Time : 546.563
    Charge : 1.16735
    Width : 6
    Flags :
]],
]]

```

Figure A.5: The trigger pulse map key contains the list of PMT hits on each DOM and on every string. The string number is represented on the first number on the OMKey class variable, and the second number represents the DOM hit in that string. The width attribute on each hit represent the PMT hit on the DOM.